

MASTER THESIS

Vibrational dynamics of CO on Pt(111) in and out of thermal equilibrium

by

Iñaki Fernandez Tena

Supervisors: Maite Alducin Ochoa & Raúl Bombín
Escudero

Date of defense: 12th of July, 2023

Index

1	Introduction and Objectives	5
2	Theory	8
2.1	Density Functional Theory	8
2.2	Density Functional Perturbation Theory (DFPT)	15
2.3	Electron-Phonon Interaction	17
2.3.1	The Electron-Phonon Matrix Element	17
2.3.2	The Phonon Self-energy	17
3	Computational Details	20
3.1	Bulk	20
3.2	Surface	22
3.3	CO on Pt(111)	22
3.4	Dynamical Matrices	25
3.5	Electron-Phonon Matrix Elements	26
3.6	Two Temperature Model	28
4	Results	31
4.1	CO Adsorption Site	31
4.2	Projected electronic DOS for CO on Pt(111)	32
4.3	Vibrational Spectra of CO on Pt(111)	34
4.4	Thermal Conditions	38
4.5	Non-Equilibrium Conditions	40
5	Summary and Conclusions	46

If it is in the reader's interest, all the code done for the figures of this work can be found in the following repository: [Master Thesis-Github](#)

1 Introduction and Objectives

Vibrations of adsorbed molecules on metallic surfaces are of great importance in various areas of research, including catalysis, materials science, and surface chemistry. Understanding the interaction between adsorbates and metal surfaces, and the effect of vibrations on this interaction, is critical for designing efficient catalysts, improving materials performance, and developing new surface-based technologies. Most of the elementary processes occurring at the gas-solid interface such as adsorption, desorption, diffusion, and reactions are closely influenced by the vibrational energy transfer of molecules adsorbed on the surfaces of metals. [1, 2].

Molecules exhibit different vibrational modes such as stretching (involving the stretching and compression of chemical bonds within a molecule), bending (the angle between the atoms on either side of the bond changes in the same/opposite way), twisting (two groups of atoms rotate around a single bond, twisting the molecule around its axis). Besides, for adlayers of molecules covering a surface these vibrational modes can occur in phase or out of phase. Specifically, the internal stretch (IS) mode in polar diatomic molecules, refers to the vibration of the atoms along the chemical bond. Along this axis there is a separation of electrical charge due to differences in electronegativity between the atoms conforming the molecule. The interest of the IS mode of polar molecules in surface science is that, being its frequency well differentiated from the rest of vibrational modes of the system, it can be easily monitored during a reaction in time-resolved infrared-visible sum-frequency generation (TR-IVSFG) experiment [1].

This technique is a second-order nonlinear optical process that converts two intense inputs lights (in this case visible and infrared) into a new light, the frequency of which is the sum of the input frequencies. In these kind of experiments, the adsorbate dynamics is initiated by a near-infrared pump laser pulse, while two additional probe pulses are next used to record with femtosecond resolution how the IS frequency and its linewidth evolves in time. It has been suggested that these changes can provide insight into the initial steps of the induced reaction, including information on the nonadiabatic coupling of IS mode with the substrate electrons [2, 3, 4, 5, 6].

An archetypal studied example are CO molecules adsorbed on metal surfaces. Usually, when the pump pulse in TR-IVSFG spectroscopy perturbs the surface of the metal, a shift in the frequency of the vibrational IS mode towards longer wavelengths is observed (redshift). It has been observed in different metals: CO/Ru(0001) [4], CO/Ir(111) [7], CO/Cu(100) [8], among others. Nonetheless, there has also been observed a blueshift (shift to a higher frequency of the IS mode) in IR spectroscopy experiments performed under thermal conditions in CO/Pd(100) [9] and CO/Ni(111) [10], as well as in TR-IVSFG spectroscopy experiments performed in CO molecules coordinated to ruthenium tetraphenylporphyrin on a Cu(110) [11].

The development of theoretical models aimed to explain the underlying processes that cause the changes in the vibrational spectra observed in this kind of experiments is an active research topic. Quite recently, Novko *et al.* [12, 13] developed a theoretical framework

based on many-body perturbation theory (MBPT) and density functional perturbation theory (DFPT) that was able to reproduce the experimental transient changes observed in CO/Cu(100) by TR vibrational spectroscopy [8]. With the same MBPT-DFPT methodology, Bombín *et al.* [14] predicted a blueshift of the IS mode in the CO/Pd(111) system. One of the characteristics of Pd(111) is that it has a pronounced sharp decrease of its density of states (DOS) at the Fermi level [14]. The authors showed that the mentioned blueshift was a direct consequence of such a sharp change in the DOS. A similar feature appears in the DOS of the Pt(111) surface [15]. This similarity motivates us to study the vibrational spectra of CO/Pt(111) using the same theoretical framework. The system is particularly interesting as only a redshift has been observed in this system via TR-IVSFG experiments [2, 6].

Platinum is a transition metal with a lattice constant of 3.92 Å [16]. Pt has a face-centered-cubic (FCC) structure. The (111) surface shows a hexagonal structure with a relatively high coordination number of nine atoms for the surface atoms. The CO/Pt(111) configuration has been widely studied. The first experimental works on the adsorption site of CO on Pt(111) date from 1970s using different techniques: High-Resolution Electron-Energy-Loss Spectroscopy (EELS) [17, 18, 19], Low Energy Electron Diffraction (LEED) [20], Infrared Reflection-Adsorption Spectroscopy (IRAS) [21, 22, 23] and X-Ray Photoelectron Spectroscopy (XPS) [24]. For coverage $\theta = 0.33$ monolayer (ML), a $\sqrt{3} \times \sqrt{3}$ structure is found. For this coverage, top sites are occupied, whereas for $\theta > 0.33$ ML bridge sites start to be occupied. Nonetheless, there has been a lot of uncertainty on how the adsorption site of CO varies with coverage. In the mentioned TR-IVSFG experiments [2, 6], the authors tried to maintain a coverage of ≈ 0.33 ML by exposing the CO/Pt(111) sample at a constant pressure in the range of 3×10^{-8} to 5×10^{-7} Torr, so that the sample must be in an Ultra-High Vacuum (UHV) chamber.

Regarding the theoretical studies on the vibrational properties of CO/Pt(111), one of the first approaches, consisting in a semi-empirical model accounting for vibrational relaxation and anharmonic coupling between phonons, was carried out by Persson *et al.* [25] in 1989. Later, calculations with a tight binding method were carried out to get some insight on the adsorption structure of CO on Ni(111), Pd(111), and Pt(111) surfaces [26]. Ni, Pd, and Pt are in the same column of the periodic table (with increasing period) so one may expect some similarities. However, the experimental evidence shows that the adsorption structures are different for each transition metal: 2-fold bridge sites on Ni(111), 3- and 2-fold sites on Pd(111), and on-top sites on Pt(111).

With the development of density functional theory (DFT) codes, in 1997 the first DFT study about CO adsorption on Pt(111) compared the dissociation of CO on Pt(111) and Ni(111) using the local density approximation (LDA)[27]. By the end of the 20th century it became manifest the failure of DFT in predicting the correct adsorption structure of CO on Pt, which has been extensively referred in the literature as the *CO puzzle*. Standard DFT calculations predict that the most stable adsorption site is in the hollow one. In the early 2000s, various studies were trying to understand this adsorption site problem [28, 29, 30]. More recently, in 2017, Janthon *et al.* [31] in a comparative study including 30 exchange-correlation functionals showed that only the M06-L functional [32] provides

the correct relative stability between the top and hollow sites. Although in the same study the authors show that when vdW dispersion is included for that functional, the prediction hollow site is the most stable one, what hints to a cancellation of errors in the M06-L prediction. In 2018, a DFT study with the nonlocal functional of Dion *et al.* [33] that includes vdW dispersion in a self-consistent manner was carried out by Gunasooriya *et al.* [34]. In this case, the correct relative stability between the top and hollow positions was achieved, although the prediction for difference of energy between the two structures is too small. Finally, in a more recent study Kundappaden *et al.* [35] compared different van der Waals functionals and showed that only vdW-DF and vdW-DF2 [36] provide the correct preference for the adsorption site.

In this work the adsorption structure for the CO/Pt(111) with a coverage of 0.33 ML has been constructed using PBE, vdW-DF and BEEF-vdW functionals¹. The surface is constructed in a $\sqrt{3} \times \sqrt{3}$ periodic cell containing a four layer Pt slab and one CO molecule. The vibrational spectra and vibrational properties are also studied. In addition, the vibrational spectra of the CO adlayer is studied under thermal and pump-probe non-equilibrium conditions. In particular, we provide a study of the IS vibrational mode of the CO/Pt(111) adsorbed at the top position by analysing the changes of its frequency shift and linewidth for thermal conditions and for different femtosecond pump pulse laser fluences.

The Master Thesis is organized as follows. An overview of the theoretical frameworks and computational tools used to calculate the electronic and phononic structures, and the effect of the electron-phonon interaction on the vibrational spectra is given in section 2. All the computational details, including the accuracy tests and the details of the two temperature model that is used to describe the perturbation that the pump laser pulse creates in the system, are described in section 3. The main results of this Master Thesis are presented and discussed in section 4. Finally, the main conclusions are summarized in section 5. In addition to this, we explain the possible studies that can be performed to complete this work.

¹As mentioned above, there are large discrepancies between different functionals for the most stable adsorption position of the CO molecule, so we use three different functionals to get a deeper analysis of our system.

2 Theory

In this section we summarize the theoretical framework that has been used in this Master Thesis.

2.1 Density Functional Theory

Kohn-Sham density functional theory (DFT) is one of the most commonly used methods to solve the “many-electron problem” in quantum mechanics. As the calculations presented here are based on DFT, we present a brief overview about this method.

The starting point is the *ab-initio* or *first principles* approach. In this case, the Hamiltonian is described by the energies and interactions of the nuclei and electrons that form the whole system and reads

$$\hat{H} = \hat{T}_n + \hat{V}_{n-n} + \hat{T}_e + \hat{V}_{n-e} + \hat{V}_{e-e} + \hat{V}_{n-field} + \hat{V}_{e-field}. \quad (1)$$

In the above equation, the operator \hat{T}_n represents the kinetic energy of the K nuclei in the system, *i.e.*,

$$\hat{T}_n = \sum_{\alpha=1}^K \frac{(-i\hbar\nabla_{\mathbf{R}_\alpha})^2}{2M_\alpha}, \quad (2)$$

where \mathbf{R}_α and M_α are the coordinate vector and mass of nucleus α , respectively, and \hbar is the reduced Plank’s constant. The operator \hat{V}_{n-n} is the interaction potential energy among the nuclei

$$\hat{V}_{n-n} = \sum_{\alpha,\beta=1;\alpha<\beta}^K \frac{Z_\alpha Z_\beta e^2}{|\mathbf{R}_\alpha - \mathbf{R}_\beta|}, \quad (3)$$

where Z_α is the atomic number of the nucleus α and e the electron charge. The operator \hat{T}_e is the kinetic energy of the n_e electrons in the system

$$\hat{T}_e = \sum_{i=1}^{n_e} \frac{(-i\hbar\nabla_i)^2}{2m_e}, \quad (4)$$

where m_e is the electron mass. The operators \hat{V}_{n-e} and \hat{V}_{e-e} represent the nucleus-electron

and electron-electron interactions that read, respectively,

$$\hat{V}_{n-e} = - \sum_{\alpha=1}^K \sum_{i=1}^{n_e} \frac{Z_{\alpha} e^2}{|\mathbf{R}_{\alpha} - \mathbf{r}_i|} \quad (5)$$

and

$$\hat{V}_{e-e} = \sum_{i,j=1:i < j}^{n_e} \frac{e^2}{|\mathbf{r}_i - \mathbf{r}_j|} . \quad (6)$$

Finally, the operators $\hat{V}_{n-field}$ and $\hat{V}_{e-field}$ represent the interaction of the nucleus and the electrons with an external electromagnetic field, respectively. If it is in the reader's interest, further discussion on the expressions for these terms ($\hat{V}_{n-field} + \hat{V}_{e-field}$) can be found in the first chapter of *Eberhard Engel and Reinier M. Dreizler* book, *Theoretical and Mathematical Physics: Density Functional Theory* [37]. However, these terms are not needed in the context of this Master Thesis. Let us remark that by using the Hamiltonian of Eq. (1), the motion for both electrons and nuclei are treated strictly as non-relativistic. For heavy atoms, relativistic effects might be important for the correction of \hat{T}_e . In addition to this, the interaction between charged particles is given by the instantaneous and spin-independent Coulomb interaction.

The simplest and most studied systems are single atoms. After transformation into the center-of-mass frame, the dynamical treatment is only required for the electrons. This can be done as the Hamiltonian can be separated into a part for the motion of the center-of-mass and the motion of electrons relative to the center-of-mass (which is essentially identical to the position of the nucleus). For polyatomic systems, *i.e.* molecules, solids,... this factorization is no longer possible, as one has to deal with the coupled dynamics of electrons and nuclei. Therefore, for the polyatomic case, the stationary Schrödinger equation reads

$$\hat{H}\Psi_a(\mathbf{R}_1, \dots, \mathbf{R}_K, \mathbf{r}_1\sigma_1, \dots, \mathbf{r}_N\sigma_N) = E_a\Psi_a(\mathbf{R}_1, \dots, \mathbf{R}_K, \mathbf{r}_1\sigma_1, \dots, \mathbf{r}_N\sigma_N), \quad (7)$$

where $\{\Psi_a\}$ and $\{E_a\}$ are the total wavefunctions and corresponding energies of the system. Here, σ_i denotes the spin state of the i^{th} electron. Usually the system that one wants to analyse has a number of particles that goes over many orders of magnitudes, so that Eq. (7) becomes unviable to solve. At this point, one has to start thinking about doing some approximations.²

The first common approximation is the Born-Oppenheimer approximation (BOA). As

²Hereinafter, we omit the spin index and indistinctly use curly brackets to denote the set of electronic and nuclear coordinates as $\{\mathbf{r}\}$ and $\{\mathbf{R}\}$.

seen in Eq. (1), there are two kinetic energies in the coupled electron-nucleus system, \hat{T}_e and \hat{T}_n , that are inversely proportional to the electron and nucleus mass, respectively. The difference between both masses (comparing, for instance, the proton and electron masses for H, *i.e.*, the lightest atom) is very large, $m_p \sim 2000 m_e$. This makes a huge difference between both kinetic energies, being $\hat{T}_e \gg \hat{T}_n$, and one can assume that electrons will adapt instantaneously to the nuclei movement. Therefore, as far as electrons are concerned, the nuclei kinetic energy term can be neglected and the nuclear coordinates can be considered fix and they can be treated as parameters. This allows us to partial decouple electrons from nuclei motion in the stationary Schrödinger equation of the full system (Eq. (7)) that now admits separate solutions for electrons and nuclei. In the end, the BOA yields two eigenvalue equations. One for the electronic Hamiltonian $\hat{H}_e = \hat{T}_e + \hat{V}_{n-e} + \hat{V}_{n-n} + \hat{V}_{e-e}$ that reads

$$\left[\hat{T}_e + \hat{V}_{n-e} + \hat{V}_{n-n} + \hat{V}_{e-e} \right] \psi_k(\{\mathbf{r}\}; \{\mathbf{R}\}) = E_k(\{\mathbf{R}\}) \psi_k(\{\mathbf{r}\}; \{\mathbf{R}\}), \quad (8)$$

where $\psi_k(\{\mathbf{r}\}; \{\mathbf{R}\})$ and $E_k(\{\mathbf{R}\})$ are the electron eigenfunctions and eigenvalues (energies) that will depend on the nuclei coordinates. Note that \hat{V}_{n-n} does not depend on the electron coordinates yielding a constant value. And another one for the nuclei in which the electronic energy acts as an effective potential:

$$\left[\hat{T}_n + E_k(\{\mathbf{R}\}) \right] \Phi_m(\{\mathbf{R}\}) = E_m \Phi_m(\{\mathbf{R}\}), \quad (9)$$

where $\Phi_m(\{\mathbf{R}\})$ and E_m are the nuclear eigenfunctions and eigenvalues, respectively.

Focusing in the electronic system, the difficulty in solving Eq. (8) comes from the electron-electron interaction term (Eq. (6)). The Hartree-Fock (HF) approximation gives us a path to overcome this problem. The idea is that each electron experiences an effective potential produced by the nucleus and the average effects of the remaining electrons. As a result, the multielectronic Hamiltonian of Eq. (8) is reduced to a sum of one-electron Hamiltonians with corresponding single-particle states $\phi_\nu(\mathbf{r}_\nu)$. In order to keep the fermionic properties of the electrons (*i.e.*, antisymmetric wavefunctions), the HF electronic wavefunction is approximated by a single Slater determinant of those single-particle states,

$$\psi(\mathbf{r}_1, \dots, \mathbf{r}_{n_e}) \approx \frac{1}{\sqrt{n_e!}} \begin{vmatrix} \phi_1(\mathbf{r}_1) & \dots & \phi_1(\mathbf{r}_{n_e}) \\ \vdots & \ddots & \vdots \\ \phi_{n_e}(\mathbf{r}_1) & \dots & \phi_{n_e}(\mathbf{r}_{n_e}) \end{vmatrix}. \quad (10)$$

The expected value of the electronic Hamiltonian through the above mentioned wave-

function yields the expected values of the kinetic energy, the external potential energy generated by the nuclei, the external classical interaction energy of the nuclei E_{n-n} , and the interaction among electrons:

$$\begin{aligned} \langle \psi | \hat{H}_e | \psi \rangle &= \sum_{\nu=1}^{n_e} \int d\mathbf{r} \phi_{\nu}^*(\mathbf{r}) \left[\frac{(-i\hbar\nabla)^2}{2m_e} - \sum_{\alpha=1}^K \frac{Z_{\alpha}e^2}{|\mathbf{R}_{\alpha} - \mathbf{r}|} \right] \phi_{\nu}(\mathbf{r}) + E_{n-n} \\ &+ \frac{1}{2} \sum_{\nu,j=1}^{n_e} \int d\mathbf{r} \int d\mathbf{r}' \phi_{\nu}^*(\mathbf{r}) \phi_j^*(\mathbf{r}') \frac{e^2}{|\mathbf{r} - \mathbf{r}'|} [\phi_{\nu}(\mathbf{r}) \phi_j(\mathbf{r}') - \phi_j(\mathbf{r}) \phi_{\nu}(\mathbf{r}')]. \quad (11) \end{aligned}$$

Notice that the expected value of the mean electron energy consists of a direct and an exchange term. The former represents the classical Coulomb interaction and is known as the Hartree energy, while the latter is a direct consequence of the antisymmetry of the wavefunction [37].

The HF approximation implements in the wavefunction the Pauli's exclusion principle via the single Slater determinant, Eq. (10). However, there is a problem, the wavefunction does not contain the correlations resulting from the interaction between the electrons: each electron simply suffers the average field of the complete electron cloud, while the actual motion of an electron depends on the individual positions of all other electrons, via the Coulomb repulsion. This interaction is the so-called Coulomb correlation. The correlation term plays an important role in many systems, so in order to take this into account, one has to go beyond the HF approximation. One alternative to go beyond HF is DFT.

Since DFT is based on the Hohenberg-Kohn (HK) theorems, we shall start the discussion on DFT by stating them [38]. These theorems ensure that a many-particle system is fully characterized by the ground state of the electron density, $n(\mathbf{r})$. In particular, the total energy of the electronic system in an external potential, v_{ext} , is a functional of the electron density,

$$E_e[n] = \langle \psi | \hat{H}_e | \psi \rangle = E_{kin}[n] + E_{e-e}[n] + E_{ext}[n]. \quad (12)$$

In our case, the external potential and corresponding energy is defined by the classical interaction among electrons and nuclei and among the nuclei themselves, $E_{ext}[n] = \langle \psi | \hat{V}_{n-e} + \hat{V}_{n-n} | \psi \rangle$.

The HK theorems are:

1. HK Theorem I:

For any system of interacting electrons in an external potential $v_{ext}(\mathbf{r})$, its ground-state electron density determines uniquely the external potential $v_{ext}(\mathbf{r})$, *i.e.*, there is a unique correspondence:

$$v_{ext}(\mathbf{r}) \iff n(\mathbf{r}) \quad (13)$$

2. HK Theorem II:

The ground state energy can be obtained variationally: The ground-state electron density $n_0(\mathbf{r})$ is the one that minimizes the total energy $E_e[n]$, *i.e.*,

$$E_e[n_0(\mathbf{r})] \leq E_e[n(\mathbf{r})] \quad (14)$$

Nevertheless, the HK theorems state nothing about the actual dependence of the kinetic energy, $E_{kin}[n]$, and of the electron-electron interaction energy, $E_{e-e}[n]$, on the electron density.

In order to make the HK theorems more practical, in 1965 *Kohn and Sham* [39] proposed a theoretical approach with the aim of minimizing $E_e[n]$, where the exact $n(\mathbf{r})$ of the interacting electrons is the same as that of a fictitious system of noninteracting electrons in an effective external potential. In this case, the electronic wavefunction is given by the Slater wavefunction of Eq. (10) and the corresponding charge density reads [38]:

$$n(\mathbf{r}) = \sum_{\nu}^{n_e} |\phi_{\nu}^{KS}(\mathbf{r})|^2, \quad (15)$$

where $\phi_{\nu}^{KS}(\mathbf{r})$ are the Kohn-Sham (KS) noninteracting orbitals. Furthermore, the total electron energy functional can be written as

$$E_e[n] = E_{kin}^0[n] + E_H[n] + E_{xc}[n] + E_{n-e}[n], \quad (16)$$

where now it is possible to calculate exactly the kinetic energy of this noninteracting system as

$$E_{kin}^0[n] = \langle \psi | \hat{T}_e | \psi \rangle = -\frac{1}{2} \sum_{\nu}^{n_e} \int d\mathbf{r} \phi_{\nu}^{KS*}(\mathbf{r}) \nabla^2 \phi_{\nu}^{KS}(\mathbf{r}), \quad (17)$$

whereas the electron-electron interaction energy is separated in two terms, the Hartree energy $E_H[n]$ that, as discussed above, represents the classical Coulomb interaction (see Eq. (11)) and the exchange and correlation energy $E_{xc}[n]$, which embodies all missing electron-electron quantum interactions of the first term, including corrections to the non-interacting kinetic energy.

Minimization of Eq. (16) leads to the following one-electron Schrödinger like equations

(e.g., see ref. [40] for a detailed derivation),

$$\left[-\frac{1}{2}\nabla^2 + v_{eff}(\mathbf{r}) \right] \phi_\nu^{KS}(\mathbf{r}) = \epsilon_\nu \phi_\nu^{KS}(\mathbf{r}) \quad (\nu = 1, \dots, n_e) , \quad (18)$$

with the effective potential being:

$$v_{eff}(\mathbf{r}) = v_{ext}(\mathbf{r}) + \int d\mathbf{r}' \frac{n(\mathbf{r}')}{|\mathbf{r} - \mathbf{r}'|} + \frac{\delta E_{xc}[n]}{\delta n(\mathbf{r})} . \quad (19)$$

Equation (18) are the so-called KS equations. Equations (18) and (19) must be solved self-consistently. A brief scheme is shown in Fig. 1. Once these equations are solved the ground-state total energy is given by [37]

$$E = \sum_{\nu=1}^{n_e} \epsilon_\nu - E_H + E_{xc} - \int d\mathbf{r} n(\mathbf{r}) v_{xc}(\mathbf{r}) . \quad (20)$$

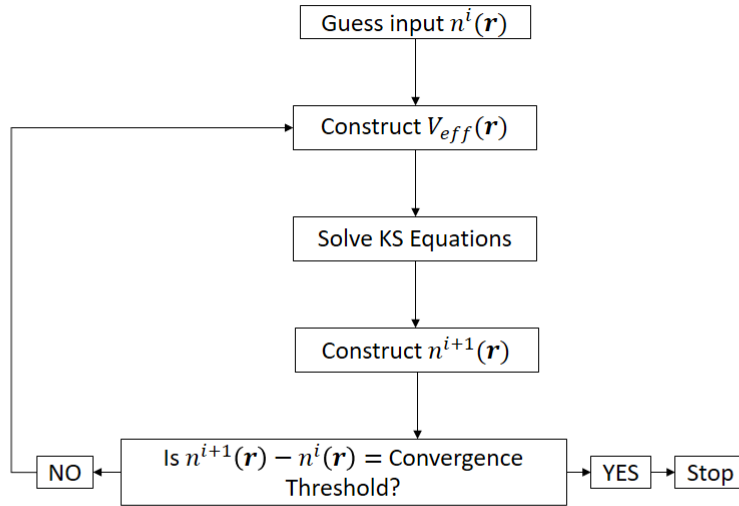


Figure 1: Flow chart of a self-consistent calculation for KS equations. The integer i in the image marks the calculation step.

Solving KS equations replaces the eigenvalue problem of Eq. (8) to the set of KS equations Eq. (18), so that the system of fully interacting electrons is replaced by the non-interacting electrons moving in an effective potential. Unfortunately, the form of the exchange and correlation density functional is unknown. Thus, only variational solutions are obtained. There are many different approaches to $E_{xc}[n]$. The first and simplest one is the local density approximation (LDA) proposed by Kohn and Sham in 1965 [39]. In this case, $E_{xc}[n]$ only depends on the value of $n(\mathbf{r})$ at each coordinate in space. LDA is derived from the equation of state of the homogeneous electron gas (HEG). In HEG, also known as the Jellium model, interacting electrons are placed in a uniform positive charge background. On the above basis, the LDA exchange and correlation density functional is written as

$$E_{xc}^{LDA}[n] = \int d\mathbf{r} n(\mathbf{r}) v_{xc}^{HEG}(n(\mathbf{r})). \quad (21)$$

The $v_{xc}^{HEG}(\mathbf{r})$ term can be separated into the exchange and correlation terms

$$v_{xc}^{HEG}(\mathbf{r}) = v_x^{HEG}(\mathbf{r}) + v_c^{HEG}(\mathbf{r}), \quad (22)$$

where the exact form for the HEG exchange part is known analytically [41]:

$$v_x^{HEG}(\mathbf{r}) = -\frac{0.4582}{r_s}, \quad (23)$$

with

$$r_s = \left[\frac{3}{4\pi n} \right]^{\frac{1}{3}} \quad (24)$$

being the Wigner-Seitz radius (i.e., the volume that the electron “occupies” at that density). The correlation contribution is obtained from Quantum Monte-Carlo simulations [42, 43]. Even if LDA qualitatively provides good results, a lot of improvements have been done in order to get more accurate exchange and correlation functionals. In the generalized gradient approximation (GGA) [44], the exchange-correlation potential depends functionally on the electron density and on its gradient:

$$E_{xc}^{GGA}[n] = \int d\mathbf{r} n(\mathbf{r}) v_{xc}(n(\mathbf{r}), \nabla n(\mathbf{r})). \quad (25)$$

The above-mentioned LDA and GGA functionals provide good solutions to many problems related to the electronic structure of solids, atoms, and small molecules. However when long-range interactions are important, the van der Waals interaction must be taken into account. In this case, the correlation term needs to be corrected by nonlocal (nl) contributions, including a $E_c^{nl}[n]$ term to the total $E_{xc}[n]$ exchange and correlation functional [33].

In this work we will use the following three exchange-correlation (xc) functionals. The GGA proposed by Perdew-Burke-Ernzerhof (PBE) [44], which is a simplified functional in which all GGA parameters are fundamental physical constants. The original van der Waals density functional (vdW-DF) proposed by Dion *et al.* [33]. And the bayesian error estimation functional (BEEF-vdW) [45] that has been adjusted over a large surface chemistry data set and also includes van der Waals corrections. The motivation to use functionals with vdW corrections is to include polarization fluctuations that in molecule-surface systems are expected to be important. One of the general purposes in this work is to determine the possible dependence of the vibrational spectra of CO/Pt(111) on the selected xc functional.

2.2 Density Functional Perturbation Theory (DFPT)

In this work we use DFPT to obtain the dynamical matrix from which the phonon spectra is calculated [16]. Here we briefly describe how dynamical matrices can be obtained in the context of DFPT.

DFPT consists in linearising up to first order in atomic displacements the KS Eqs. (18), specifically, evaluating the perturbation in the effective potential of Eq. (19) and in the electron density in Eq. (15). These linearised terms can be expressed as [46]:

$$\Delta n(\mathbf{r}) = \sum_{\alpha} \frac{\partial n(\mathbf{r})}{\partial \boldsymbol{\tau}_{\alpha}} \Delta \boldsymbol{\tau}_{\alpha}, \quad (26)$$

$$\Delta v_{eff}(\mathbf{r}) = \sum_{\alpha} \frac{\partial v_{eff}(\mathbf{r})}{\partial \boldsymbol{\tau}_{\alpha}} \Delta \boldsymbol{\tau}_{\alpha}, \quad (27)$$

where $\boldsymbol{\tau}_{\alpha}$ is the displacement of atom α . The above two expression allows us to write the first-order perturbation KS equations [46]:

$$\left[-\frac{1}{2} \nabla^2 + v_{eff}(\mathbf{r}) - \epsilon_{\mu\mathbf{k}} \right] \Delta \phi_{\mu\mathbf{k}}(\mathbf{r}) = - [\Delta v_{eff}(\mathbf{r}) - \Delta \epsilon_{\mu\mathbf{k}}] \phi_{\mu\mathbf{k}}(\mathbf{r}), \quad (28)$$

where the first-order correction to the effective potential is

$$\Delta v_{eff}(\mathbf{r}) = \Delta v_{ext}(\mathbf{r}) + \int d\mathbf{r}' \frac{\Delta n(\mathbf{r}')}{|\mathbf{r} - \mathbf{r}'|} + \frac{\delta v_{xc}[n(\mathbf{r})]}{\delta n(\mathbf{r})} \Delta n(\mathbf{r}) \quad (29)$$

and $\Delta \epsilon_{\mu\mathbf{k}} = \langle \phi_{\mu\mathbf{k}} | \Delta v_{eff} | \phi_{\mu\mathbf{k}} \rangle$. Equation (28) defines a set of self-consistent equations similar to the KS equations.

The procedure in DFPT can be summarized as:

- Calculate the unperturbed KS eigenstates and eigenvalues of the system.
- Solve the DFPT equations self-consistently to obtain simultaneously the perturbed eigenstates and perturbation potentials due to atomic displacements.
- Compute the second-order change in the total energy of the system induced by the atomic displacements (Hessian matrix, matrix of force constants in the harmonic approximation) [46]:

$$\begin{aligned} C_{xy}^{i,j}(\boldsymbol{\tau}^0; t - t') &= \frac{\partial^2 E(\boldsymbol{\tau}^0)}{\partial \tau_x^i(t) \partial \tau_y^j(t')} = \int d\mathbf{r} \left[\frac{\partial n(\mathbf{r}, \boldsymbol{\tau}^0)}{\partial \tau_y^j(t')} \right] \left[\frac{\partial v_{ext}(\mathbf{r})}{\partial \tau_x^i(t)} \right] + \\ &+ \int d\mathbf{r} n(\mathbf{r}, \boldsymbol{\tau}^0) \left[\frac{\partial^2 v_{ext}(\mathbf{r})}{\partial \tau_y^j(t') \partial \tau_x^i(t)} \right] + \left[\frac{\partial^2 V_{n-n}(\mathbf{r})}{\partial \tau_y^j(t') \partial \tau_x^i(t)} \right], \quad (30) \end{aligned}$$

where $\boldsymbol{\tau}^0$ is the position at equilibrium of the unit cell, x and y denote the Cartesian components of the atomic displacement vectors, i, j are used to label the ions and $C_{xy}^{i,j}$ are the so-called dynamical matrix elements, which relates atomic displacements to forces.

- Fourier transform the force constant matrix to obtain the dynamical matrix element [46]:

$$C_{xy}^{i,j}(\mathbf{q}, \omega) = \int dt \sum_{\boldsymbol{\tau}^0} e^{i(\omega t - \mathbf{q}\boldsymbol{\tau}^0)} C_{xy}^{i,j}(\boldsymbol{\tau}^0; t), \quad (31)$$

where \mathbf{q} is the crystal momentum.

- Finally, diagonalize the dynamical matrix to obtain the phonon frequencies $\omega(\mathbf{q})$:

$$[\mathbf{C}(\mathbf{q}) - \omega^2(\mathbf{q})\mathbf{I}] \mathbf{u}(\mathbf{q}) = 0, \quad (32)$$

where \mathbf{I} is the identity matrix, and $\mathbf{u}(\mathbf{q})$ is the eigenvector of the dynamical matrix corresponding to the phonon mode with wavevector \mathbf{q} .

2.3 Electron-Phonon Interaction

2.3.1 The Electron-Phonon Matrix Element

In this section we consider a system of non-interacting electrons and non-interacting phonons in which the electron-phonon interaction can be treated as a perturbation. In second quantization, the total Hamiltonian reads [46]:

$$\hat{H} = \sum_{n\mathbf{k}} \varepsilon_{n\mathbf{k}} \hat{c}_{n\mathbf{k}}^\dagger \hat{c}_{n\mathbf{k}} + \sum_{\mathbf{q}\nu} \hbar\omega_{\mathbf{q}\nu} (\hat{a}_{\mathbf{q}\nu}^\dagger \hat{a}_{\mathbf{q}\nu} + 1/2) + N_p^{-1/2} \sum_{\mathbf{k}, \mathbf{q}, n, n', \nu} g_\nu^{nn'}(\mathbf{k}, \mathbf{q}) \hat{c}_{n\mathbf{k}+\mathbf{q}}^\dagger \hat{c}_{n'\mathbf{k}} (\hat{a}_{\mathbf{q}\nu} + \hat{a}_{-\mathbf{q}\nu}^\dagger), \quad (33)$$

where $\hat{c}_{n\mathbf{k}+\mathbf{q}}^\dagger$, $\hat{c}_{n'\mathbf{k}}$ and $\varepsilon_{n\mathbf{k}}$ is the creation operator, the annihilation operator and the single-particle eigenvalue of an electron in the state with crystal momentum index \mathbf{k} in the band index n , $\hat{a}_{\mathbf{q}\nu}$ and $\hat{a}_{-\mathbf{q}\nu}^\dagger$ are the creation and annihilation operators of a phonon with crystal momentum \mathbf{q} in the branch ν , N_p is the number of unit cells and $g_\nu^{nn'}(\mathbf{k}, \mathbf{q})$ is the electron-phonon matrix element. The electron-phonon matrix element (carried out within one unit cell of the crystal, “uc”) can be expressed as [46]:

$$g_\nu^{nn'}(\mathbf{k}, \mathbf{q}) = \frac{1}{\sqrt{2M_\nu\omega_{\mathbf{q}\nu}}} \langle \mathbf{u}_{n\mathbf{k}+\mathbf{q}} | \Delta_{\mathbf{q}\nu} V_{eff} | \mathbf{u}_{n'\mathbf{k}} \rangle_{uc}, \quad (34)$$

where M_ν is the effective mass for each phonon with crystal momentum \mathbf{q} and branch ν , $\omega_{\mathbf{q}\nu}$ is the frequency of the phonon mode ν , $u_{n'\mathbf{k}}$ and $u_{n\mathbf{k}+\mathbf{q}}$ are the Bloch-periodic components of the Kohn-Sham electron wavefunctions and $\Delta_{\mathbf{q}\nu} V_{eff}$ is the phonon-induced variation of the self-consistent potential experienced by the electrons.

The first line in Eq. (33), describes the non-interacting electron and phonon systems and the second the first-order electron-phonon coupling Hamiltonian, which reads,

$$\hat{H}_{ep} = N_p^{-1/2} \sum_{\mathbf{k}, \mathbf{q}, n, n', \nu} g_\nu^{nn'}(\mathbf{k}, \mathbf{q}) \hat{c}_{n\mathbf{k}+\mathbf{q}}^\dagger \hat{c}_{n'\mathbf{k}} (\hat{a}_{\mathbf{q}\nu} + \hat{a}_{-\mathbf{q}\nu}^\dagger). \quad (35)$$

2.3.2 The Phonon Self-energy

The changes that are induced in the IS mode of CO on Pt(111) due to the electron-phonon coupling are calculated within many-body perturbation theory in terms of the phonon

self-energy [12, 13, 46, 47]. In particular, following Novko *et al.* [12, 13, 47], the phonon self-energy is obtained up to second-order in the electron-phonon coupling, *i.e.*,

$$\pi_\lambda(\omega, \mathbf{q}) \approx \pi_\lambda^{[1]}(\omega, \mathbf{q}) + \pi_\lambda^{[2]}(\omega, \mathbf{q}), \quad (36)$$

where λ , ω , and \mathbf{q} denote the index, energy, and momentum of the phonon mode, respectively. Since in the vibrational spectroscopy experiments the CO molecules are initially prepared with their IS mode vibrating in phase ($\mathbf{q} = 0$) by illuminating them with an IR pulse, for simplicity, all the expressions will be written hereafter for this particular case. Thus, the expression for the first-order term $\pi_\lambda^{[1]}(\omega)$, which accounts for the electron-hole pair (de)excitations, reads [47]

$$\pi_\lambda^{[1]}[\omega; T_e] = \sum_{nn'\mathbf{k}\sigma} \left| g_\lambda^{nn'}(\mathbf{k}, 0) \right|^2 \frac{f(\varepsilon_{n\mathbf{k}}) - f(\varepsilon_{n'\mathbf{k}})}{\omega + \varepsilon_{n\mathbf{k}} - \varepsilon_{n'\mathbf{k}} + i\eta}, \quad (37)$$

where the summation in σ accounts for the spin degree of freedom, $g_\lambda^{nn'}(\mathbf{k}, \mathbf{q} = 0)$ are the electron-phonon matrix elements, $f(\varepsilon) = 1/[e^{\beta(\varepsilon - \mu(T_e))} + 1]$ is the Fermi-Dirac distribution function (where $\beta = 1/(k_B T_e)$ and k_B is the Boltzmann constant), T_e is the electronic temperature and $\mu(T_e)$ is the chemical potential at T_e .

The second-order term comes from the idea that the IS mode can excite electron-hole pairs that experience a second scattering process with a low energy phonon mode. This term is denoted as the electron-mediated phonon-phonon coupling (EMPPC) and reads [12]

$$\begin{aligned} \pi_\lambda^{[2]}[\omega; T_e; T_l] = & - \sum_{nn'\mathbf{k}\sigma, \lambda'\mathbf{k}'} \left| g_\lambda^{nn'}(\mathbf{k}, 0) \right|^2 \left(1 - \frac{g_\lambda^{n'n'}(\mathbf{k}', 0)}{g_\lambda^{nn'}(\mathbf{k}, 0)} \right) \left| g_{\lambda'}^{nn'}(\mathbf{k}, \mathbf{q}') \right|^2 \\ & \times \sum_{s, s' = \pm 1} \frac{f(\varepsilon_{n\mathbf{k}}) - f(\varepsilon_{n'\mathbf{k}'} - s' s \omega_{\mathbf{q}'\lambda'})}{\varepsilon_{n\mathbf{k}} - (\varepsilon_{n'\mathbf{k}'} - s' s \omega_{\mathbf{q}'\lambda'})} \frac{s [n_b(s \omega_{\mathbf{q}'\lambda'}) + f(s' \varepsilon_{n'\mathbf{k}'})]}{\omega [\omega + i\eta + s'(\varepsilon_{n\mathbf{k}} - \varepsilon_{n'\mathbf{k}'} + s \omega_{\mathbf{q}'\lambda'})]}, \end{aligned} \quad (38)$$

where $\mathbf{q}' = \mathbf{k}' - \mathbf{k}$, the function $n_b(\omega_{\mathbf{q}\lambda}) = 1/(e^{\beta \omega_{\mathbf{q}\lambda}} - 1)$ is the Bose-Einstein distribution function, where $\beta = 1/(k_B T_l)$ and T_l is the lattice temperature.

Notice that in the case of pump-probe vibrational spectroscopy, the perturbation created by the pump pulse is described in terms of time-dependent electronic and lattice temperatures, $T_e(t)$ and $T_l(t)$, that are obtained by solving the Two-Temperature Model (TTM) (see

section 3.6). In that case, we will calculate the transient changes in the vibrational spectra because these are the properties that are usually reported by experimentalists. From the phonon self-energy it is straightforward to obtain the frequency shift

$$\Delta\omega(t) \approx \Re[\pi_\lambda(\omega, t)] - \Re[\pi_\lambda(\omega, 0)] \quad (39)$$

and the linewidth

$$\gamma(t) = -2\Im[\pi_\lambda(\omega, t)], \quad (40)$$

$$\Delta\gamma = -2(\Im[\pi_\lambda(\omega; t)] - \Im[\pi_\lambda(\omega; 0)]) \quad (41)$$

due to the electron-phonon interaction in the IS mode of the CO molecule. As the phonon self-energy of Eq. (36) consist of first- and second-order terms, $\Delta\omega(t) = \Delta\omega^{[1]}(t) + \Delta\omega^{[2]}(t)$ and $\gamma(t) = \gamma^{[1]}(t) + \gamma^{[2]}(t)$, we shall also analyse the contributions to the frequency shift and the linewidth coming from the first and second-order terms:

$$\Delta\omega^{[1]}(t) \approx \Re[\pi_\lambda^{[1]}(\omega, t)] - \Re[\pi_\lambda^{[1]}(\omega, 0)] \quad (42)$$

$$\Delta\omega^{[2]}(t) \approx \Re[\pi_\lambda^{[2]}(\omega, t)] - \Re[\pi_\lambda^{[2]}(\omega, 0)] \quad (43)$$

$$\gamma^{[1]}(t) = -2\Im[\pi_\lambda^{[1]}(\omega, t)] \quad (44)$$

$$\gamma^{[2]}(t) = -2\Im[\pi_\lambda^{[2]}(\omega, t)] \quad (45)$$

3 Computational Details

In this work, the electronic structure has been evaluated with DFT and the dynamical matrices and phonon perturbation potentials with DFPT using the *QUANTUM ESPRESSO* (QE) first principles package [48, 49]. All calculations have been performed for three different xc functionals: Perdew-Burke-Ernzerhof (PBE), van der Waals-Density Functional (vdW-DF), and Bayesian Error Estimation Functional-van der Waals (BEEF-vdW). The pseudopotentials for C, O, and Pt were those developed by A. dal Corso [50]. These pseudopotentials are generated with the projector augmented-wave (PAW) method [51]. Those calculations related to the electron-phonon interaction have been carried out using the Electron-phonon Wannier (EPW) code package. Here we summarize how we have adjusted the different parameters needed for the calculations.

3.1 Bulk

Platinum is a transition metal with a face-centered cubic (fcc) structure. However, in the $\{111\}$ direction, it exhibits a hexagonal structure. In order to obtain accurate electronic calculations, it is important to optimize the following two factors: (i) the \mathbf{K} points mesh and (ii) the kinetic energy cutoff for the plane waves basis set, as QE expands the KS wavefunctions into plane waves. Once these two optimization steps are done, one can proceed to calculate the bulk lattice parameter a for each functional.

In our case, we started by optimizing the \mathbf{K} -points mesh. During this optimization process the values of the lattice parameter and the energy cutoff are fixed. In particular, we use as lattice parameter the experimental value $a = 3.92 \text{ \AA}$ [16] and as energy cutoff the value suggested in the pseudopotential ($E_{\text{cut}} = 39 \text{ Ry}$). The energy of bulk Pt, $E_{\text{bulk}}(K \times K \times K)$, is calculated self-consistently for increasing values of the \mathbf{K} -points mesh until achieving a certain energy convergence criteria that we decide to be $E_{\text{bulk}}(K \times K \times K) - E_{\text{bulk}}(32 \times 32 \times 32) < 10^{-4} \text{ Ry}$. Next, we proceed with the energy cutoff convergence and calculate the Pt bulk energy for increasing values of E_{cut} . During these calculations a is fixed to the experimental lattice parameter as before and the \mathbf{K} -points mesh is fixed to the optimized one. The optimization process finishes when the self-consistent Pt bulk energy differs in less than 10^{-4} Ry from the value obtained with an energy cutoff of 400 Ry, $E_{\text{bulk}}(E_{\text{cut}}) - E_{\text{bulk}}(400) < 10^{-4} \text{ Ry}$.

The results of the \mathbf{K} -points mesh and E_{cut} convergence calculations are depicted in Figs. 2(a) and (b), respectively. Based on these convergence calculations, the selected kinetic energy cutoff is $E_{\text{cut}} = 210 \text{ Ry}$ and the \mathbf{K} -points mesh is set to $16 \times 16 \times 16$. Using these values we next proceed to calculate the bulk lattice parameter for each of the three xc functionals.

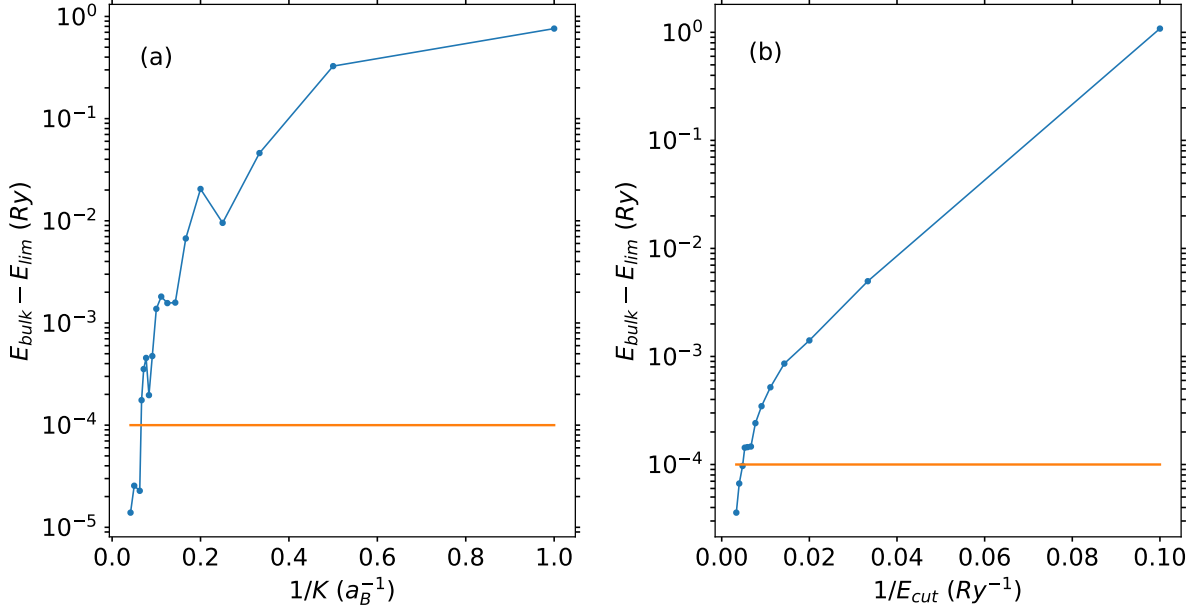


Figure 2: Differences in energy, $E_{\text{bulk}} - E_{\text{lim}}$ against (a) the inverse of the \mathbf{K} -points mesh and (b) the inverse of the kinetic energy cutoff E_{cut} . In (a) E_{lim} is E_{bulk} calculated with a $32 \times 32 \times 32$ \mathbf{K} -points mesh and in (b) E_{lim} is E_{bulk} calculated with $E_{\text{cut}} = 400$ Ry. The orange line represents the desired convergence energy value of 10^{-4} Ry (≈ 1 meV). In both figures the y scale is logarithmic.

Figure 3 shows the dependence of the Pt bulk energy on the value of the lattice parameter for each xc functional. The theoretical lattice parameter for each xc functional is the value at which the corresponding $E_{\text{bulk}}(a)$ curve reaches the minimum. A summary of the results can be found in Table 1.

Functional	$a(a_B)$	a (Å)	Error
PBE	7.52	3.97	1.27 %
vdW-DF	7.63	4.03	2.80 %
BEEF-vdW	7.57	4.00	2.04 %

Table 1: Lattice parameter in Bohr radius $a(a_B)$, in angstrom $a(\text{\AA})$ and the relative error respect to the experimental value $a^{\text{exp}} = 3.92$ Å [16] evaluated for the three xc functionals.

As expected the different functionals provide slightly different predictions for the bulk lattice constant [15].

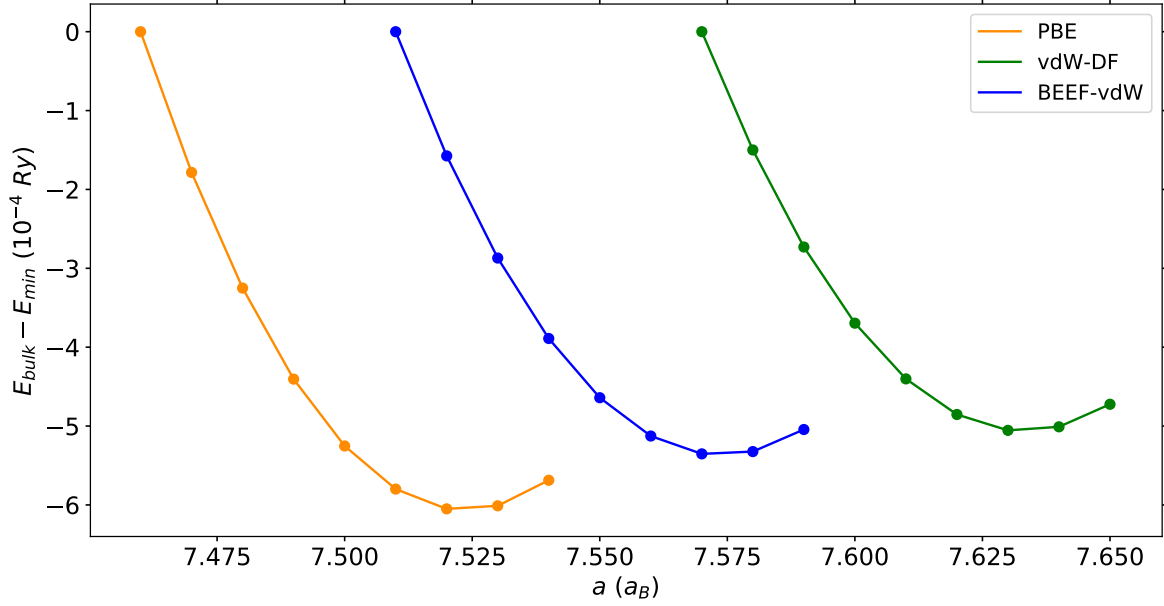


Figure 3: Energy of bulk Pt as a function of the lattice parameter for PBE (orange), vdW-DF (green) and BEEF-vdW (blue). For each xc functional the reference bulk energy E_{min} is that of the smallest a value used in the corresponding optimization calculations.

3.2 Surface

The Pt(111) surface is modeled in a $\sqrt{3} \times \sqrt{3}$ supercell containing 4 atomic layers, with a vacuum layer of 20.00 Å for BEEF-vdW, 19.89 Å for PBE and 20.18 Å for vdW-DF between periodic slabs. Each layer contains 3 atoms, thus making a total of 12 atoms in the slab. We set as initial guess of the interlayer distance the theoretical value $a/\sqrt{3}$. Next, the position of all the Pt atoms is relaxed until all the interatomic force components are smaller than $F = 10^{-5} \text{ Ry}/a_B$. The results for each interlayer distance are summarized in Table 2 together with available experimental data. As in the case of the lattice constant, the smallest values correspond to PBE followed by BEEF-vdW, and vdW-DF in this order. Nonetheless, all the values agree reasonably well with the available experimental data, in particular with the values reported in Experiment 1 [52]. In the three cases, the differences of the bulk interlayer distances are less than 1%. One of the most remarkable results here is that the three xc functionals predict that $d_{23} < d_{12}$, as in experiments.

3.3 CO on Pt(111)

For each xc functional, we calculate the adsorption properties for four different positions of the carbon monoxide on the surface: top (atop one Pt atom of the first layer), bridge (between two Pt atoms of the first layer), fcc (over one Pt atom of the third layer), and

Functional	d_{12} (Å)	d_{23} (Å)	d_{bulk} (Å)
PBE	2.31	2.28	2.29
vdW-DF	2.34	2.30	2.33
BEEF-vdW	2.33	2.29	2.31
Experiment 1 [52]	2.29 ± 0.01	2.27 ± 0.03	-
Experiment 2 [53]	2.285 ± 0.010	2.245 ± 0.013	-

Table 2: Interlayer distance of the first and second, d_{12} , the second and the third layer, d_{23} , and bulk interlayer distances, $d_{\text{bulk}} = a/\sqrt{3}$ in angstrom $a(\text{\AA})$ for each xc functional and for two experimental results [52, 53].

hcp (over one Pt atom of the second layer). The coverage of the system is $\theta = 0.33$ ML, thus we have only one CO molecule in the first layer. An schematic image of the four cases on the Pt(111) surface can be observed in Fig. 4.

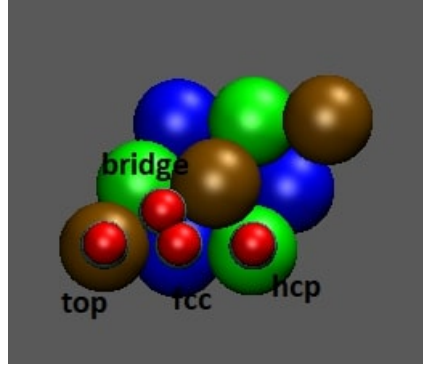


Figure 4: Sketch of the top view of CO adsorbed at top, bridge, fcc, and hcp sites in the Pt(111) surface. First layer in brown, second layer in green and third layer in blue.

Using the relaxed Pt(111) surface, we put our CO on different adsorption positions and we relax the whole system. As in the previous steps, we optimize: (i) The \mathbf{K} points mesh and (ii) the kinetic energy cutoff. In this case, we also optimize (iii) the kinetic energy cutoff for charge density and potential, E_{cutrho} . Here we try to follow the suggestion of QE to maintain $E_{\text{cutrho}} \approx 4E_{\text{cut}}$. The \mathbf{K} points mesh must have a structure of $X \times Y \times 1$, since the system is not periodic in Z direction.

We follow the same procedure as in the bulk optimization, section 3.1. In the present case, the optimization process finishes when the differences $E_{\text{surface}} - E_{\text{lim}}$ are below 10^{-3} Ry.

The results of the \mathbf{K} -points mesh, E_{cut} , and E_{cutrho} convergence are depicted in Figs. 5(a), (b) and (c), respectively. Based on these convergence calculations, the selected parameters are: $\mathbf{K}_{\text{POINTS}} = 6 \times 6 \times 1$, $E_{\text{cut}} = 92$ Ry and $E_{\text{cutrho}} = 410$ Ry. These parameters are obtained by putting the CO molecule on top position at a distance $d(\text{Pt-C}) = 1.83$ Å and $d(\text{C-O}) = 1.15$ Å [31]. We have to remark here that we will use these converged values for the three xc functionals.

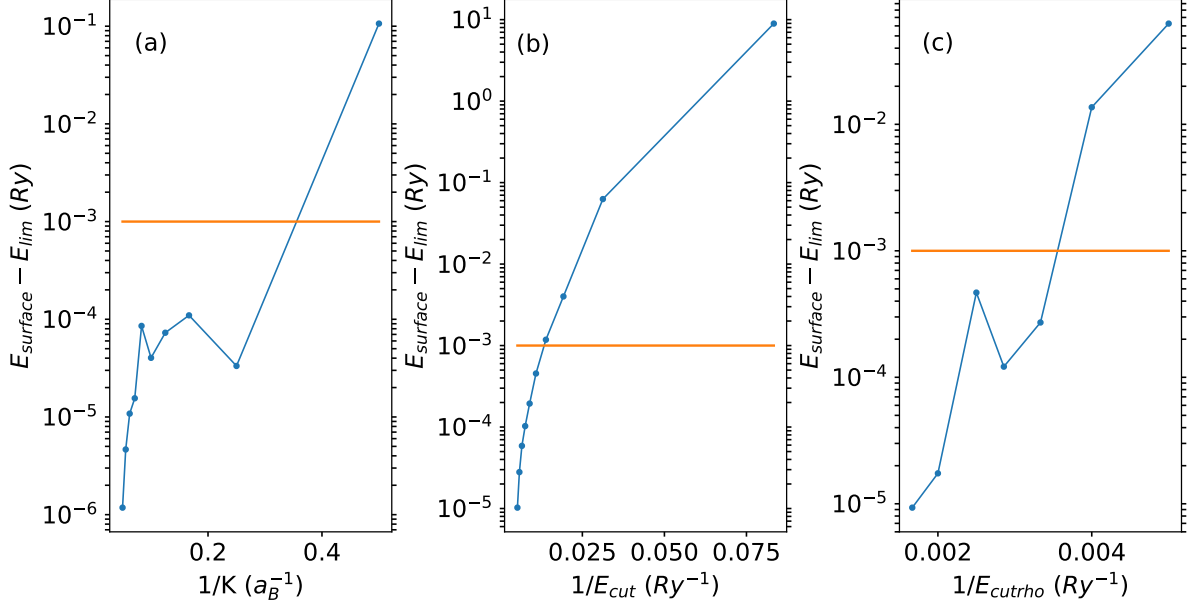


Figure 5: Differences in energy, $E_{\text{surface}} - E_{\text{lim}}$ against (a) the inverse of the \mathbf{K} -points mesh, (b) the inverse of the kinetic energy cutoff E_{cut} , and (c) the inverse of the kinetic energy cutoff for charge density and potential, E_{cutrho} . In (a) E_{lim} is E_{surface} calculated with a \mathbf{K} points mesh $22 \times 22 \times 1$, in (b) E_{lim} is E_{surface} calculated with $E_{\text{cut}} = 212$ Ry, and in (c) E_{lim} is E_{surface} calculated with $E_{\text{cutrho}} = 700$ Ry. The orange line represents the desired convergence energy value of 10^{-3} Ry. In three cases the y scale is logarithmic.

In Table 3 we summarize the DFT predictions for $d(\text{Pt-C})$ for CO adsorbed on the different positions. We also include experimental measurements for CO on top and bridge sites [54]. We relax the atoms of the supercell for each CO molecule position until the interatomic force is below 10^{-5} Ry/ a_B .

Functional	$d_{\text{Pt-C}}^{\text{top}}$ (\AA)	$d_{\text{Pt-C}}^{\text{bridge}}$ (\AA)	$d_{\text{Pt-C}}^{\text{fcc}}$ (\AA)	$d_{\text{Pt-C}}^{\text{hcp}}$ (\AA)
PBE	2.06	1.65	1.36	1.35
vdW-DF	2.09	1.70	1.36	1.37
BEEF-vdW	2.06	1.66	1.35	1.35
Experiment [54]	1.85 ± 0.10	1.55 ± 0.10	—	—

Table 3: Distances between the last platinum layer respect to the C atom for each CO adsorption position computed for each xc functional. The experimental values are taken from [54]. Distances in \AA .

For top position, $d(\text{Pt-C})$ distances have a relative error of $\approx 5\%$. For the bridge position, we obtain relaxed positions within the experimental results for PBE and BEEF-vdW, while we obtain a relative error of $\approx 3\%$ for vdW-DF. Overall, DFT systematically overestimates these measures.

In Table 4 we summarize the DFT predictions for $d(\text{C-O})$ for CO adsorbed on the different positions. We also include experimental measurements for top and bridge [54]. We relax

the atoms of the supercell for each CO molecule position until we have an interatomic force below 10^{-5} Ry/ a_B .

Functional	d_{C-O}^{top} (Å)	d_{C-O}^{bridge} (Å)	d_{C-O}^{fcc} (Å)	d_{C-O}^{hcp} (Å)
PBE	1.15	1.17	1.18	1.18
vdW-DF	1.15	1.17	1.18	1.18
BEEF-vdW	1.15	1.16	1.18	1.17
Experiment [54]	1.15 ± 0.10	1.15 ± 0.10	—	—

Table 4: Distances between the C atom respect to the O atom for each CO adsorption position computed for each xc functional. The experimental values are taken from [54]. Distances in Å.

For top position, we obtain relaxed positions within the experimental results. For bridge position, we also obtain relaxed positions within the experimental results for BEEF-vdW, while we get a relative error of 0.9% for PBE and vdW-DF. A discussion about the adsorption site of the CO molecule on Pt(111) surface will be done in section 4.1.

Finally, the energy of the relaxed CO molecule in vacuum is necessary to obtain the adsorption energy for each position, as shown in Eq. (49) below. Therefore, we relax the CO molecule position until we have an interatomic force below 10^{-5} Ry/ a_B . The obtained values are summarized for each functional in Table 5.

Functional	d_{C-O}^{Vacuum} (Å)
PBE	1.14
vdW-DF	1.14
BEEF-vdW	1.13

Table 5: Interatomic distances between the C atom respect to the O atom for each xc functional. Distances in Å.

3.4 Dynamical Matrices

To obtain the phononic dispersion and DOS we make use of the dynamical matrices which are computed using the *PHonon* QE package that uses DFPT. The dynamical matrices, Eq. (31), were obtained in a Γ -centered $6 \times 6 \times 1$ q -grid. We have 14 atoms in our surface, thus we obtain 42 modes. As a sanity check the calculations obtained with DFPT are repeated for a bigger \mathbf{K} -points mesh $8 \times 8 \times 1$ in the self-consistent DFT calculation, to ensure that we obtain a converged result with respect to the charge density. Phonon dispersion for $6 \times 6 \times 1$ (blue lines) and $8 \times 8 \times 1$ (orange dots) have been plotted in Fig. 6. The differences between the frequencies for both \mathbf{K} points meshes are below 1 meV.

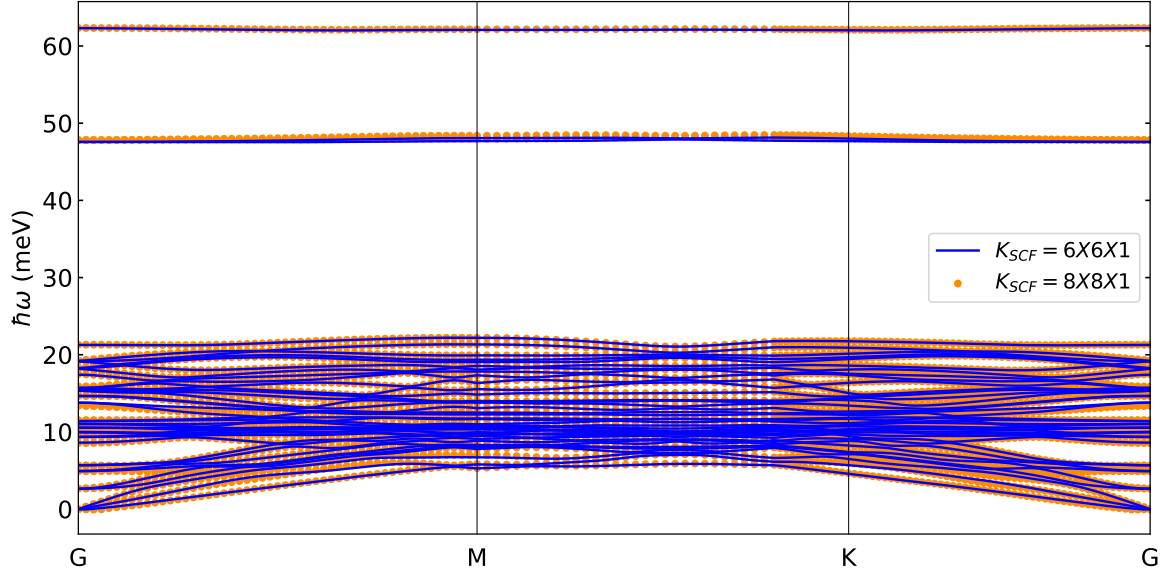


Figure 6: Phonon dispersion relation for two different \mathbf{K} -points meshes, $6 \times 6 \times 1$ (blue lines) and $8 \times 8 \times 1$ (orange dots). In this plot we use PBE. The frequencies are in meV.

3.5 Electron-Phonon Matrix Elements

We used the electron phonon Wannier (EPW) code to evaluate the electron-phonon matrix elements $g_{\nu}^{nn'}(\mathbf{k}, \mathbf{q})$ [55, 56]. This code allows us to evaluate the electron-phonon matrix elements using as an input the electronic energy levels computed with DFT $\varepsilon_{\mu,\mathbf{k}}$, and the phonon energies $\omega_{\nu,\mathbf{q}}$ and perturbation potentials obtained with DFPT. Furthermore, it takes advantage of the properties of localized Wannier functions to interpolate the electron-phonon matrix elements in a fine \mathbf{k} and \mathbf{q} grids. A Wannier function, associated with a band n , can be obtained via a unitary transformation of the Bloch state $|u_{n\mathbf{k}}\rangle$ as

$$|w_{\mathbf{R}n}\rangle = \frac{V}{(2\pi)^3} \int_{BZ} d\mathbf{K} |u_{n\mathbf{K}}\rangle e^{-i\mathbf{K}\cdot\mathbf{R}}, \quad (46)$$

where V is the real-space primitive cell volume, \mathbf{R} is a Bravais lattice vector, and the integral is over the first Brillouin zone (BZ).

To obtain the MLWFs first, we compute the electronic density in a $6 \times 6 \times 1$ \mathbf{K} -grid by performing a self-consistent DFT calculation. Subsequently, the band structure of the system is computed in a positive defined \mathbf{K} -grid containing 144 \mathbf{K} -points. The requirement of evaluating the band structure in a positive defined \mathbf{K} -grid is imposed by the implementation of the Wannierization process in the EPW code. With this input, $\varepsilon_{\mu,\mathbf{k}}$, we use the EPW code to compute the MLWFs [57]. The selected columns of density matrix (SCDM) algorithm [55] is used to chose the initial projections. It is worth noticing that the bands of an electronic system are entangled in general, which might give place to large errors in the energy levels during the Wannierization process with respect to the

DFT values. With this in mind we have performed Wannierizations considering different number of bands $n_{n \in [76, 85]}$. For each Wannierization, only the exact number of bands that we want to consider are included as an input. We find that best interpolation of the band structure is obtained for $n_{\text{bnd}} = 81$. In the left plot of Figs. 7, 8, and 9 we compare the DFT band structure across the Gamma-M-K-G line in the first BZ computed with DFT and interpolating it with MLWFs. On the right plot of the same figures we plot the differences $|(\varepsilon_{\mu, \mathbf{k}}^{\text{DFT}} - \varepsilon_{\mu, \mathbf{k}}^{\text{MLWFs}})|$. From the plots it is clear that small differences, < 20 meV, appear for energies below the Fermi level. Above the Fermi level, differences are larger but still only a few points exhibit an error larger than 40 meV.

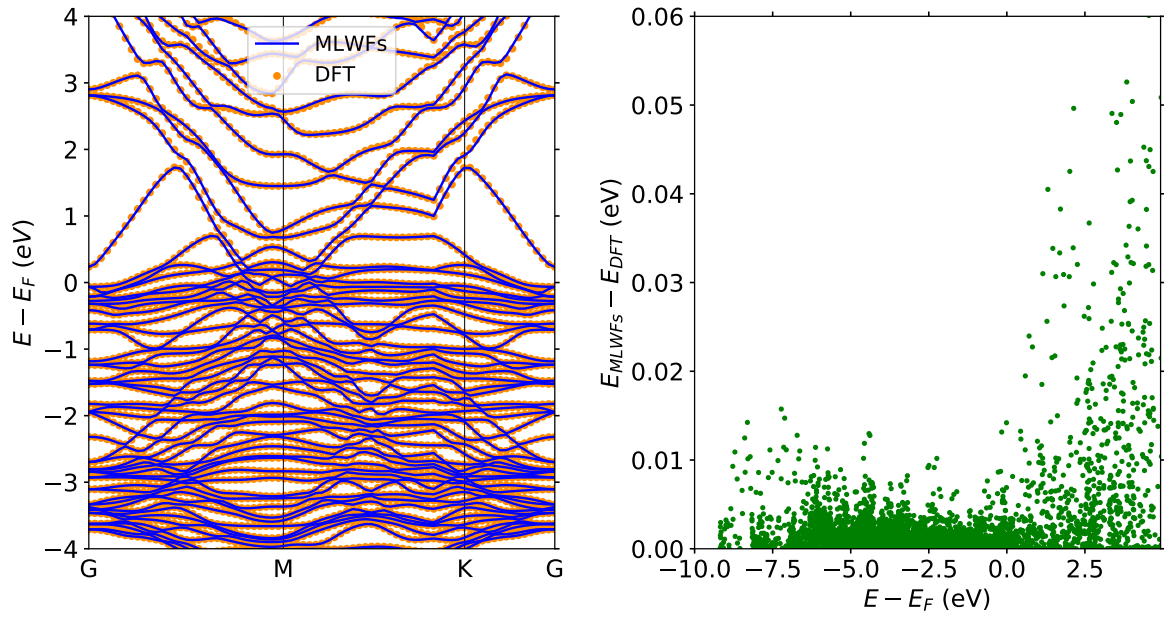


Figure 7: Band structure calculated with DFT (orange dots) and with MLWFs (solid blue) and the error between the energies of both band structures (green dots). The band structure is shown in an energy range $E \in [-4\text{eV}, 4\text{eV}]$, putting the zero energy at the Fermi level. In this plot we use PBE. We compute the band structure at 77 \mathbf{K} -points.

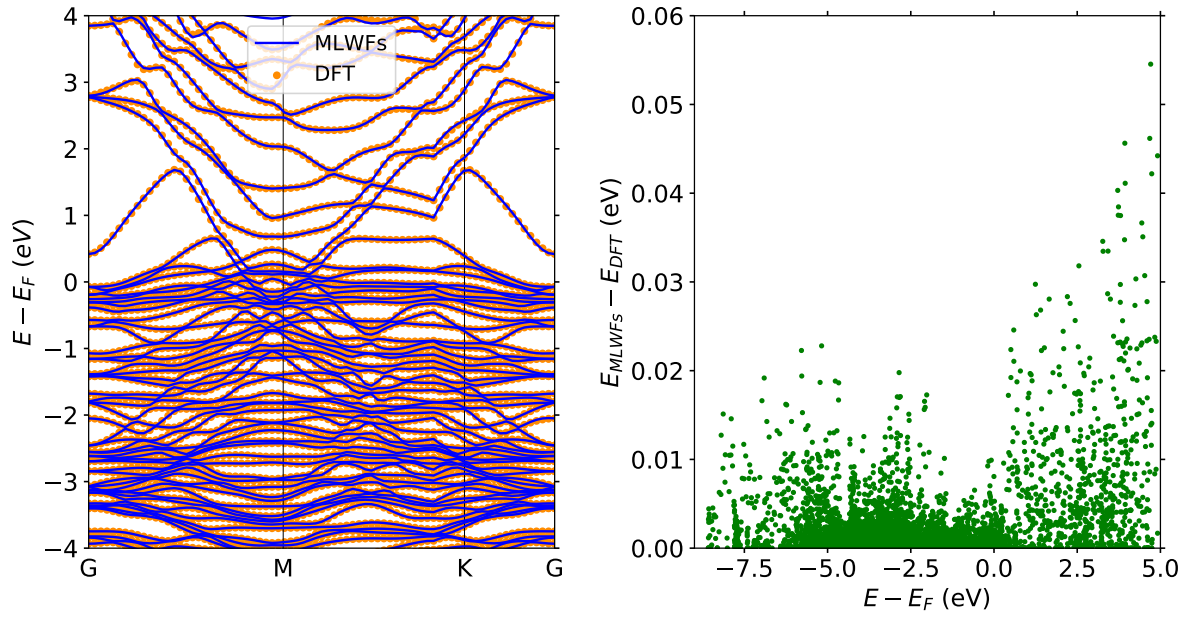


Figure 8: Same as Fig. 7 but calculated with *vdW-DF*.

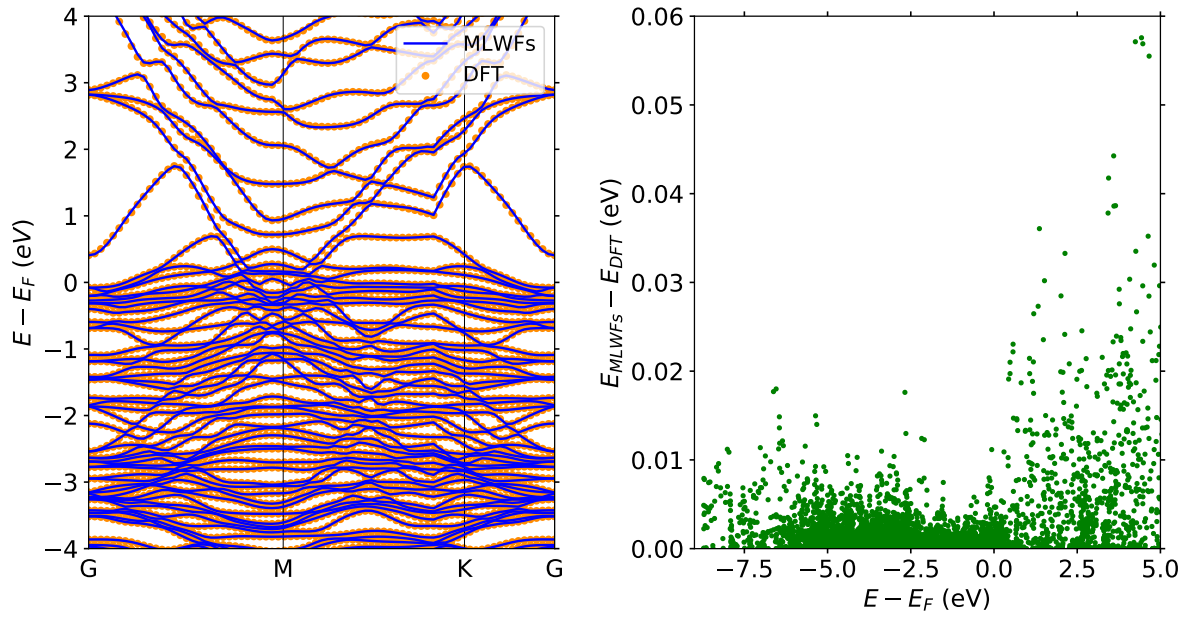


Figure 9: Same as Fig. 7 but calculated with *BEEF-vdW*.

3.6 Two Temperature Model

The two-temperature model (TTM) [58] is a widely used model to describe the effect of intense short laser pulses in metal surfaces. The TTM, describes the energy exchange between two thermal baths in a metal, one describing the electrons (which has an associated

temperature, $T_e(t)$) and the other one describing the lattice vibrations (which has an associated temperature, $T_l(t)$). The interaction between the two baths is described by a system of two coupled partial differential equations [14]:

$$\begin{aligned} C_e \frac{\partial T_e}{\partial t} &= \frac{\partial}{\partial z} \left(\kappa_e \frac{\partial T_e}{\partial z} \right) - G(T_e - T_l) + S(z, t) \\ C_l \frac{\partial T_l}{\partial t} &= G(T_e - T_l), \end{aligned} \quad (47)$$

where t denotes time, z the spatial direction perpendicular to the surface plane, C_e is the volumetric heat capacity of the electrons, C_l is the volumetric heat capacity of the lattice vibrations in the metal, κ_e is the thermal conductivity of electrons in the metal, G is the electron-phonon energy exchange coupling constant of the metal and $S(z, t)$ is the laser source term.

TTM assumes that the energy of the pulse is adsorbed at $z = 0$ and $t = 0$. We can remark that the time evolution of the lattice temperature only depends on the electron-phonon interaction and not directly on the laser. This occurs because the energy of the laser is of \approx eV, while the phonons of the surface have an energy around \approx 50 meV. Therefore, the laser source term $S(z, t)$ only enters in the equation describing the time evolution of the electronic temperature. This laser term will create a fast peak in the electronic temperature at the early times t . Once the energy of the laser is absorbed by the surface electrons, this energy is dissipated into the material and towards the ions. The energy is driven inside the material via the thermal conductivity of the electrons (the gradient in z -direction: $\kappa_e \frac{\partial T_e}{\partial z}$) and towards the ions via transferring energy to phonons (the third term of the first equation: $-G(T_e - T_l)$).

In TTM there are some input parameters that are required before solving the system of Eqs. (47). The $S(z, t)$ parameter is related to the laser source term, which is modeled with the following form [59]:

$$S(z, t) = \frac{\alpha_\lambda F}{2\Delta t} e^{-\alpha_\lambda z} \text{sech}^2 \left(\frac{t}{\Delta t} \right), \quad (48)$$

with α_λ being the light absorption coefficient of the metal for a source of wavelength λ , Δt the full width at half maximum of the temporal profile of the laser pulse, and F the absorbed fluence.

All the calculations presented in section 4.5 have been performed for the experimental pump pulse used in Ref. [2] to investigate the transient changes in the vibrational spectra of CO/Pt(111) at 0.33 ML, namely, a 400 nm pulse of 150 fs duration. The values of the lattice heat capacity for the Pt(111) surface, $C_l(T)$, are taken from experiments [60], whereas the values for G , $C_e(T)$, and κ_e correspond to first principles calculations performed by Lin. *et al.* [61] for Pt(111).

Figure 10 shows the TTM prediction of $T_e(t)$ and $T_l(t)$ for the Pt(111) surface and the three different laser fluences that will be used in section 4.5. We can directly observe that the electronic and lattice temperatures grow with the fluence so that higher values are obtained when the fluence is larger. Following the completion of the pulse, both temperatures gradually equilibrate at approximately the instant at which T_l reaches its maximum value. The peak values of $T_e(t)$ and $T_l(t)$ are $T_e(0.05 \text{ ps}) = 2900 \text{ K}$ and $T_l(1 \text{ ps}) = 428 \text{ K}$ for $F = 40 \text{ J/m}^2$; $T_e(0.08 \text{ ps}) = 4600 \text{ K}$ and $T_l(1.7 \text{ ps}) = 639 \text{ K}$ for $F = 80 \text{ J/m}^2$; and $T_e(0.1 \text{ ps}) = 6200 \text{ K}$ and $T_l(2.2 \text{ ps}) = 864 \text{ K}$ for $F = 130 \text{ J/m}^2$. Notice that in the case that we consider, the lattice temperature never excess the melting temperature of platinum, which is around 2045 K [16].

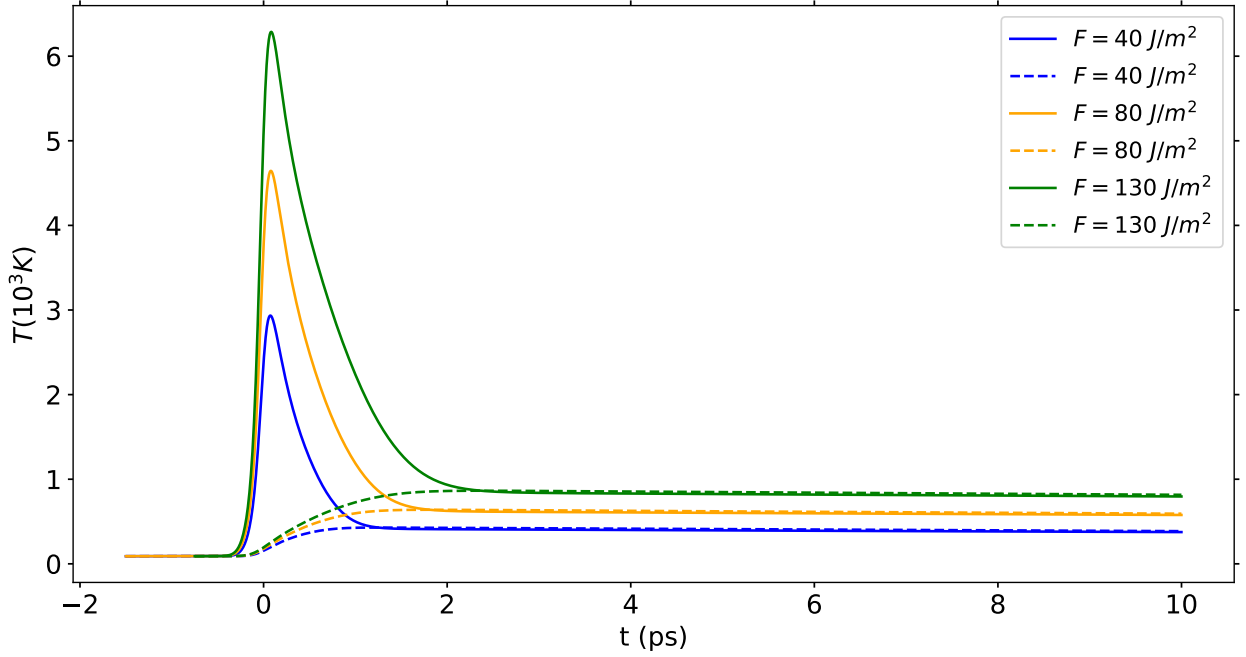


Figure 10: *Electronic (solid lines) and lattice (dashed lines) temperatures calculated with TTM for Pt(111) and laser pulses of 400 nm, 150 fs duration, and absorbed laser fluences: $F = 40 \text{ J/m}^2$ (blue), $F = 80 \text{ J/m}^2$ (orange), and $F = 130 \text{ J/m}^2$ (green). In all cases the maximum of the laser pulse hits the surface at $t = 0 \text{ ps}$.*

4 Results

In this section we present the results obtained in this Master Thesis.

4.1 CO Adsorption Site

In order to identify the energetically favorable adsorption site of CO on Pt(111), we calculate the adsorption energy E_{ads} for each of the four positions considered in this study (top, bridge, hcp, and fcc, see Fig. 4). In particular, the adsorption energy is calculated as

$$E_{\text{ads}}^i = E_{\text{CO/Pt}}^i - E_{\text{Pt}} - E_{\text{CO}} \quad (49)$$

where $E_{\text{CO/Pt}}$ is the energy of the relaxed structure of CO/Pt(111), i is the index to denote the position of CO on the surface, E_{Pt} is the energy of the relaxed structure of Pt(111), and E_{CO} is the energy of the relaxed CO molecule in vacuum. The structural parameters for CO/Pt(111), Pt(111), and the CO molecule in vacuum can be found in Tables 2, 3, 4, and 5. The obtained adsorption energies for each CO position and xc functional are summarized in Table 6.

Functional	$E_{\text{ads}}^{\text{top}}$ (eV)	$E_{\text{ads}}^{\text{bridge}}$ (eV)	$E_{\text{ads}}^{\text{fcc}}$ (eV)	$E_{\text{ads}}^{\text{hcp}}$ (eV)
PBE	-1.57	-1.61	-1.62	-1.64
vdW-DF	-1.32	-1.27	-1.24	-1.21
BEEF-vdW	-1.37	-1.38	-1.39	-1.36
Experiment [20]	-1.17	-	-	-
Experiment [62]	-1.55	-	-	-

Table 6: Adsorption energies obtained using Eq. (49) for each CO position and different xc functionals. For comparison, the experimental values from Refs. [20, 62] are also provided. All energies are in eV.

The energetically favored adsorption sites predicted by PBE, vdW-DF, and BEEF-vdW are hcp, top, and fcc sites, respectively. From the three xc-functionals, only vdW-DF is able to predict correctly the adsorption site identified in experiments for a coverage of 0.33 ML [20, 62]. In fact, the work by P. Janthon *et al.* [31] showed that the fcc position is the most favourable adsorption site for many of the xc functionals. In our case, the differences in E_{ads} between hcp and fcc are of ≈ 0.03 eV for the three xc functionals.

As already mentioned, it can be seen in the literature that with most of the functionals the larger adsorption energy is obtained in the hollow position, specifically at fcc. In our case, for the PBE we obtain that the most favourable adsorption site is hcp. The (small) discrepancies with respect to previous works may be explained in terms of the larger cut-

off, larger **K**-point set and stricter criteria for the ionic forces during the relaxation process.

Regarding the experimental adsorption energies [20, 62], there is a non-negligible difference between both values of about 0.4 eV. In our case, the vdW-DF and BEEF-vdW adsorption energies for the top site lie within the two experimental values, while the PBE E_{ads} agrees well with the experimental value of Ref. [62], being the difference of 0.02 eV only.

4.2 Projected electronic DOS for CO on Pt(111)

In Refs. [63, 64] it is shown that the DOS of CO/Pt(111) is very different when CO is adsorbed on either the top site or on the other sites (fcc, hcp, and bridge). The reason for this is that on top the CO molecule binds strongly to the d_{z^2} orbital of the Pt atom just below it. As a result of this binding, the projected DOS of the d_{z^2} orbital shifts to lower energies.

Motivated by these two studies, which were performed with PBE and the hybrid PBE0 xc functionals [65], we consider meaningful to verify whether our PBE calculations reproduce the same observations. The total DOS and the projected DOS onto s (purple) and d orbitals ($d_{x^2-y^2}$ in orange, $d_{zx} + d_{zy}$ in red, and d_{z^2} in green) centered at the nearest Pt atom in the topmost layer as well as projections onto CO molecular orbitals (MO) with σ (black), π_x (red), and π_y (blue) character are shown in Figs. 11 and 12 for CO adsorbed at the top and on the hcp site, respectively (the corresponding relaxed PBE adsorption configurations are described in Table 6). Note that in $\text{CO}_{\text{top}}/\text{Pt}(111)$ the nearest Pt is precisely the atom on which CO adsorbs, whereas in $\text{CO}_{\text{hcp}}/\text{Pt}(111)$ the projection is done on one of the three equidistant Pt atoms surrounding the CO_{hcp} molecule. Furthermore, the CO MOs with σ character are formed by combining the projections of the p_z and s atomic orbitals of carbon and oxygen atoms. The MOs with π_x character are obtained by adding the p_x orbitals of C and O, while the MOs with π_y character result from the combination of the p_y orbitals.

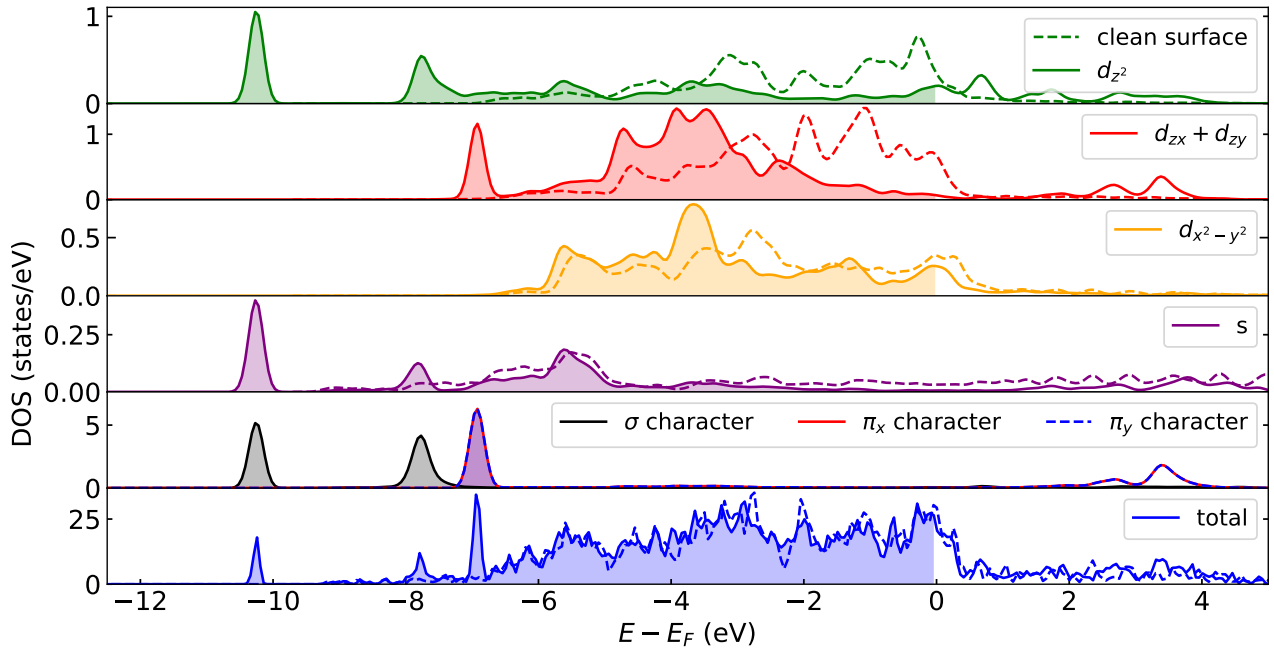


Figure 11: Total DOS (blue) and projected DOS, d_{z^2} (green), $d_{zx} + d_{zy}$ (red), $d_{x^2-y^2}$ (orange), s (purple) and CO molecular MOs with σ (black), π_x (red) and π_y (blue) character for the Pt atom beneath the CO molecule adsorbed on top position. Dashed lines represent the same Pt projections for the clean surface. The blurred colors in each projected DOS show the electronic occupied states. DOS calculated with PBE and with a denser \mathbf{K} -points mesh $12 \times 12 \times 1$.

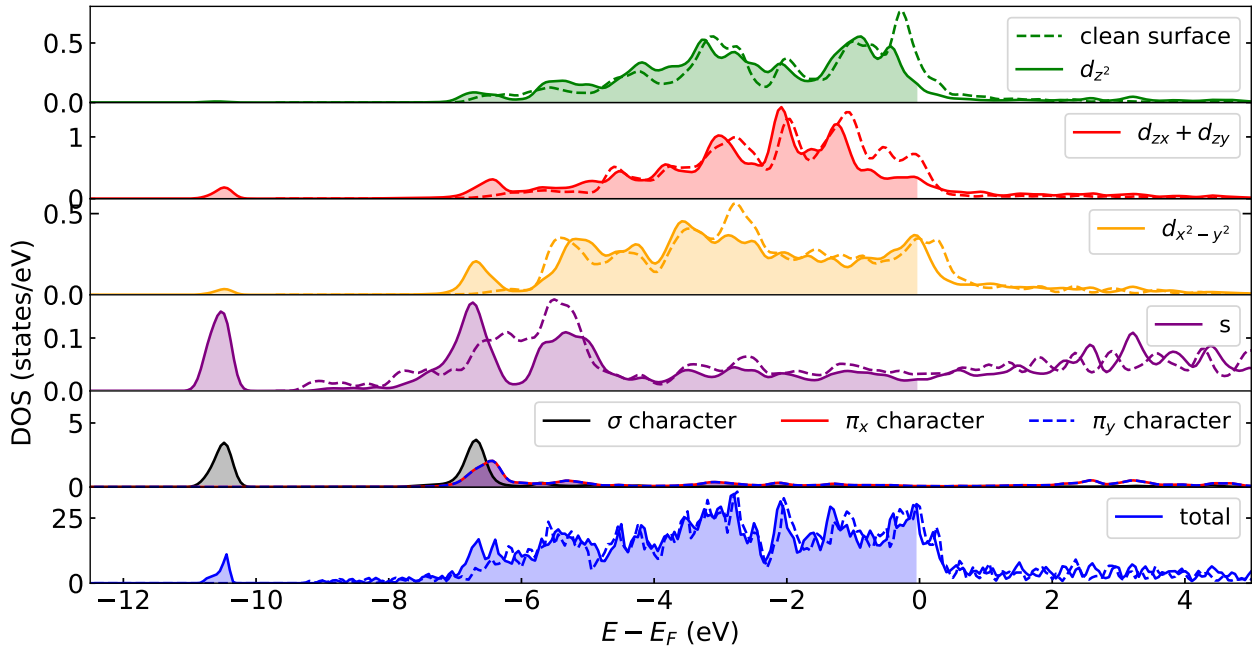


Figure 12: Same as Fig. 11 for CO adsorbed on a hcp site. The projected DOS are for one of the nearest Pt atoms in the topmost layer interacting most with CO.

On the one hand, we observe that the DOS projected onto the d_{z^2} orbital of the nearest Pt atom is shifted to lower energies when the CO molecule is adsorbed on top (take as a reference the dashed lines of the plots, which represent the projections for the clean surface). On the other hand, in the hcp case we do not observe this energy shift of the projected DOS of the d_{z^2} orbital. The d_{z^2} orbital is centred on the platinum atom and has a lobed shape. The lobes of the d_{z^2} orbital point directly along the z-axis and are symmetrically oriented. This orientation causes the binding of CO with the d_{z^2} orbital. When the CO is adsorbed on hcp, the molecule is located between the platinum atoms of the surface, which causes it not to couple with the d_{z^2} orbital of these Pt atoms. In conclusion, the shift of the d_{z^2} orbital to lower energies is caused by the adsorption position of the CO molecule.

Moreover, when the CO molecule is adsorbed on top position, the primary orbital interaction (due to their symmetry) is observed between the CO MO possessing σ character and the s and d_{z^2} orbitals of platinum (black, purple, and green peaks located at about -10.2 eV and -7.7 eV). Additionally, we notice that the CO MOs with π_x and π_y character (red and dashed blue peaks located at -6.9 eV) predominantly interact with the $d_{zx} + d_{zy}$ orbitals of Pt, which are clearly shifted to lower energies because of this interaction (compare the red solid and red dashed lines showing the $d_{zx} + d_{zy}$ projections when CO is or not adsorbed, respectively). Conversely, in the case of CO adsorbed on hcp, we observe interaction between the CO MO with σ character and the s orbital of Pt. Furthermore, there is a minor interaction between the CO MOs with π_x and π_y character and the $d_{zx} + d_{zy}$ and $d_{x^2-y^2}$ orbitals of Pt. Notably, the coupling between the CO MOs and the d_{z^2} orbital of Pt is absent.

4.3 Vibrational Spectra of CO on Pt(111)

Unless otherwise stated, the vibrational properties presented in this section and in sections 4.4 and 4.5 correspond to CO adsorbed on the top site [CO_{top}/Pt(111)]. Figures 13, 14, and 15 show the total phonon DOS and the CO-projected phonon DOS calculated with PBE, vdW-DF, and BEEF-vdW, respectively. The blue shaded area represents the total phonon DOS, while the orange shaded area represents the projection onto the CO vibrational modes. Qualitatively, there are common features among the three phonon DOS. Phonons associated to the Pt(111) surface appear in the range $\omega \approx [0 - 170] \text{ cm}^{-1}$ and overlap with the frustrated translation modes of CO. The rest of CO modes are well separated in energy from the Pt(111) phonons and appear as three distinct peaks. The IS mode, located around $\omega_{IS} \approx [2000 - 2065] \text{ cm}^{-1}$, is completely decoupled from the rest of the vibrational modes (note that the x-axis is shortened in the range $\omega \in [550 - 1900] \text{ cm}^{-1}$ to facilitate visualisation). At intermediate energies the vibrational spectra are dominated by a well defined vibrational modes (which are not easy to identify directly) and the ES modes, the energy of the former being about 100 cm^{-1} smaller than for ES with the three xc functionals. The vibrational modes are identified using the [dynmat.x](#) postprocessing program included in QE, which allows us to plot the forces acting on each atom.

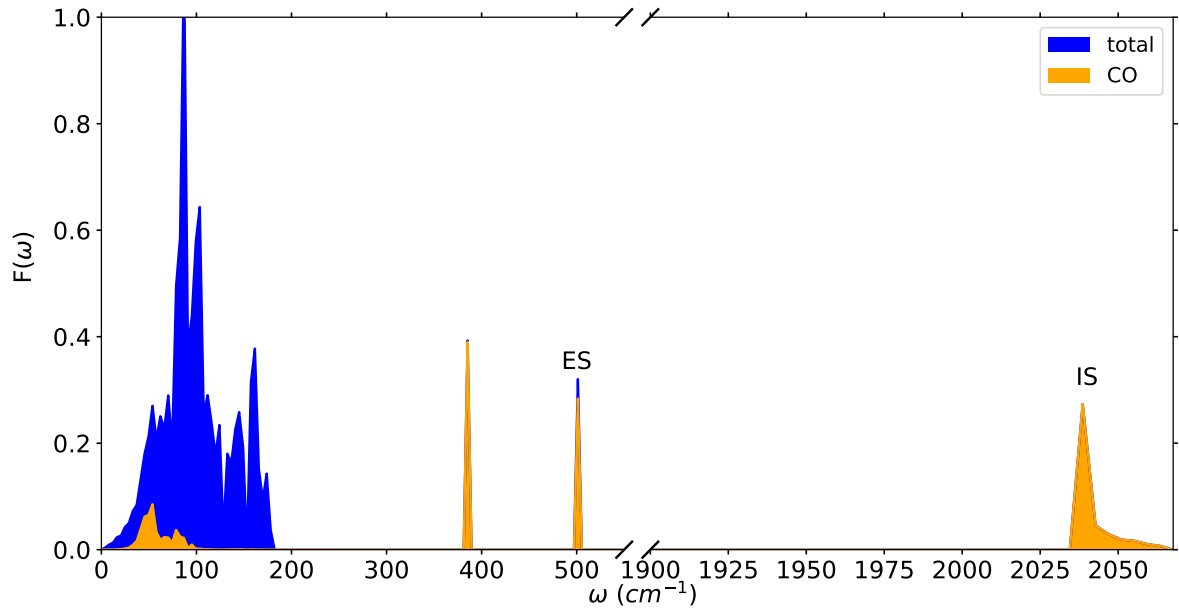


Figure 13: *Phonon DOS of $\text{CO}_{\text{top}}/\text{Pt}(111)$ calculated with PBE using a $10 \times 10 \times 1$ q-grid. Total DOS in blue and the DOS projected onto the CO modes in orange. In the projected DOS only the projections onto the CO internal stretch (IS) and the CO external stretch (ES) modes are clearly identified. The rest are not easy to identify directly.*

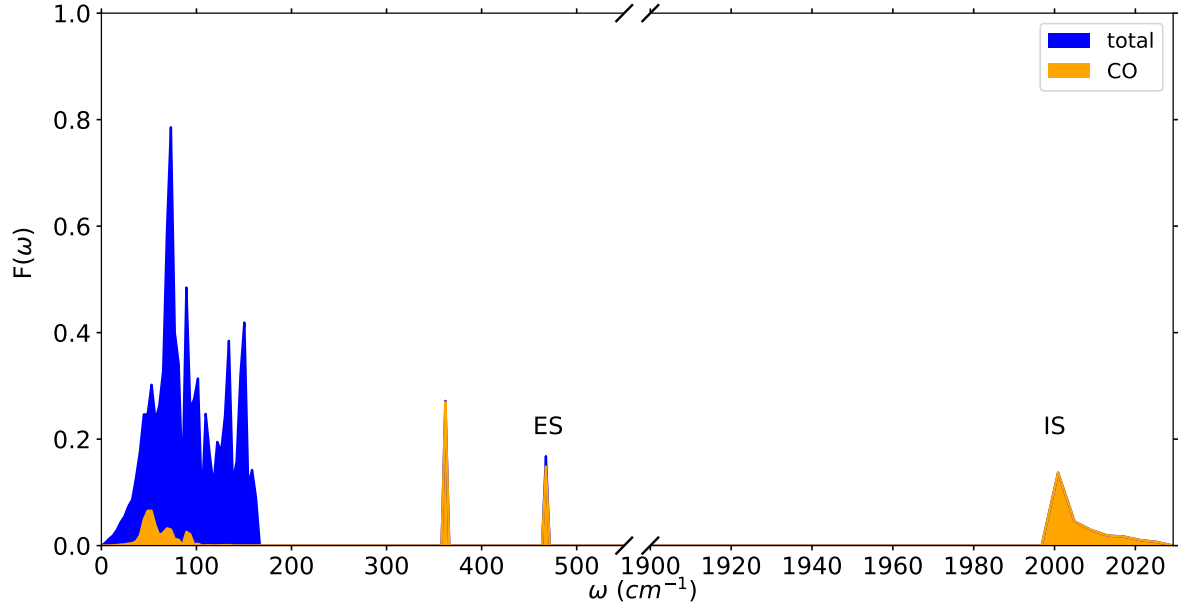


Figure 14: *Same as Fig. 13 but calculated with vdW-DF.*

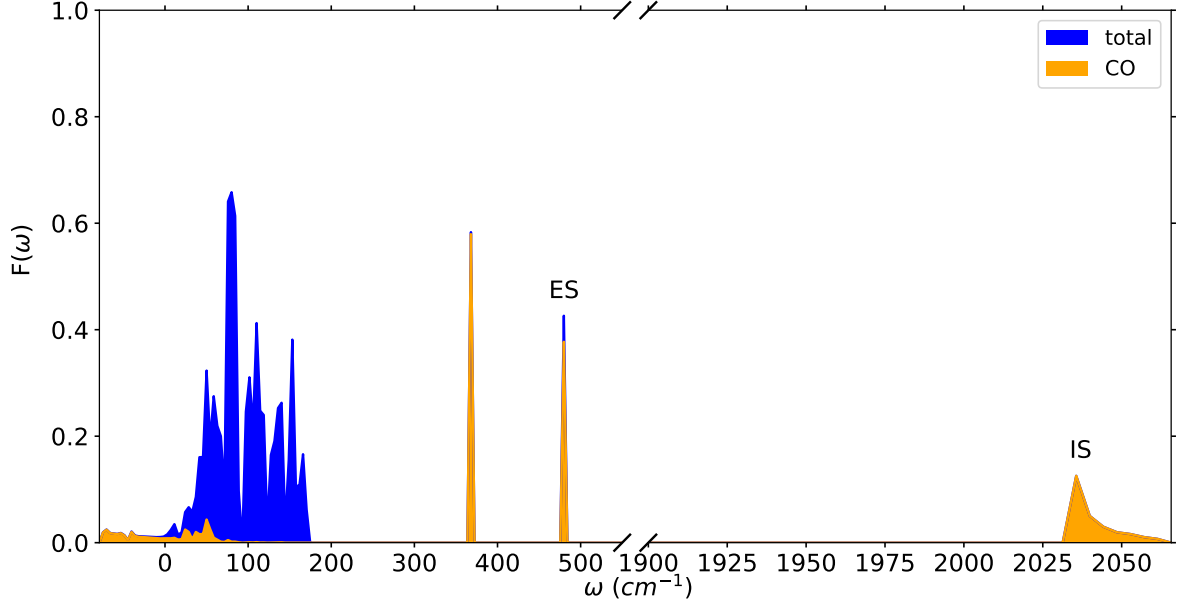


Figure 15: Same as Fig. 13 but calculated with BEEF-vdW.

The values of the IS and ES energies obtained with each xc functional are compared in Table 7 with available experimental data. The $q = 0$ values, corresponding to the highest frequency of the interval are marked in blue in the table, as they are the ones that should be compared with experimental measurements. The smallest difference between the theoretical and experimental energies for the IS mode is obtained with PBE, while for the ES mode it is obtained with vdW-DF. Note, however, that the results by Gajdos *et al.* [63] are for 0.25 ML with the CO adsorbed on top position, while our results are for 0.33 ML.

Functional	ω_{IS} (cm^{-1})	Error (%)	ω_{ES} (cm^{-1})	Error (%)
PBE	2038-2067	1.57	512	8.20
vdW-DF	2000-2029	3.38	467	0.65
BEEF-vdW	2035-2065	1.66	479	1.91
Experiment [63]	2100	—	470	—

Table 7: Energy of the CO internal stretch ω_{IS} and CO external stretch ω_{ES} modes obtained with the different xc functionals for $CO_{top}/Pt(111)$. In each case, the relative error respect to the corresponding experimental value of Ref. [63] is also provided (only for $q = 0$ values). Note however that the fact that the experimental coverage is 0.25 ML could also contribute to the difference between theory and experiments. In blue the frequencies of the IS mode corresponding to the value $q = 0$. All frequencies in cm^{-1} .

If we look closely at the BEEF-vdW phonon DOS (Fig. 15), we note that there are vibrational states at negative energies. This feature is readily observed in the phonon spectra plotted in Fig. 16(a) in the range $\omega = [-100, 500] cm^{-1}$. There are two phonon branches with negative energies that correspond to the frustrated translation modes of CO. In principle, negative energies (or imaginary frequency modes) are associated with

unstable vibrational modes (negative second derivatives of the potential energy). However, we cannot discard that these first two negative modes may simply be a numerical error in our DFPT calculations.

Figure 16(b) shows the phonon spectra in the same energy range for the CO molecule adsorbed on fcc, which is the most favourable adsorption position for BEEF-vdW (see Table 6). In this case, there are not negative vibrational modes, which means that we obtain a stable adsorption position for the $\text{CO}_{\text{fcc}}/\text{Pt}(111)$ configuration. Compared to $\text{CO}_{\text{top}}/\text{Pt}(111)$, the energies of the IS and ES modes are slightly lower, $\omega_{\text{IS}} \approx 1782 \text{ cm}^{-1}$ and $\omega_{\text{ES}} \approx 340 \text{ cm}^{-1}$. Gajdos *et al.* [63] reported IS energies within the range $\omega_{\text{IS}}^{\text{exp}} \in [1736 - 1855] \text{ cm}^{-1}$ for different monolayer experiments using Reflection Adsorption Infrared Spectroscopy (RAIRS). The authors also performed theoretical calculations that yielded $\omega_{\text{IS}} = 1793 \text{ cm}^{-1}$ and $\omega_{\text{ES}} = 352 \text{ cm}^{-1}$. As argued by the authors, the frequencies of the IS and ES modes tend to decrease to lower values when the adsorption position of CO changes from top to fcc. This trend has been observed by different authors on different surfaces and it is also observed in our vibrational mode values.

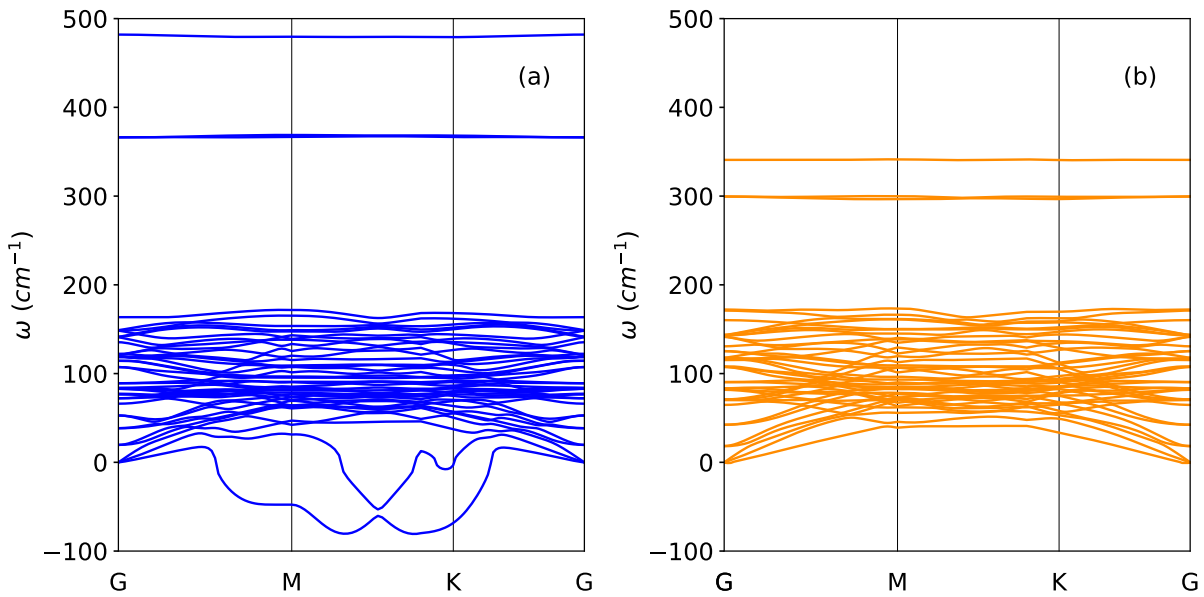


Figure 16: Phonon dispersion for $\text{CO}/\text{Pt}(111)$ in (a) top (blue) and (b) fcc (orange) configurations calculated with BEEF-vdW using a \mathbf{q} -grid of $6 \times 6 \times 1$.

Finally, to ensure that we do not obtain unstable vibrational modes for the $\text{CO}_{\text{top}}/\text{Pt}(111)$ configuration with PBE and vdW-DF, we show their phononic dispersion within the energy range $\omega = [-100, 500] \text{ cm}^{-1}$ in Figs. 17(a) and (b), respectively. In both cases, all the phonon branches take positive energy values, confirming that CO on top is stable for both functionals, even if the $\text{CO}_{\text{top}}/\text{Pt}(111)$ configuration is not the energetically favored adsorption position for PBE.

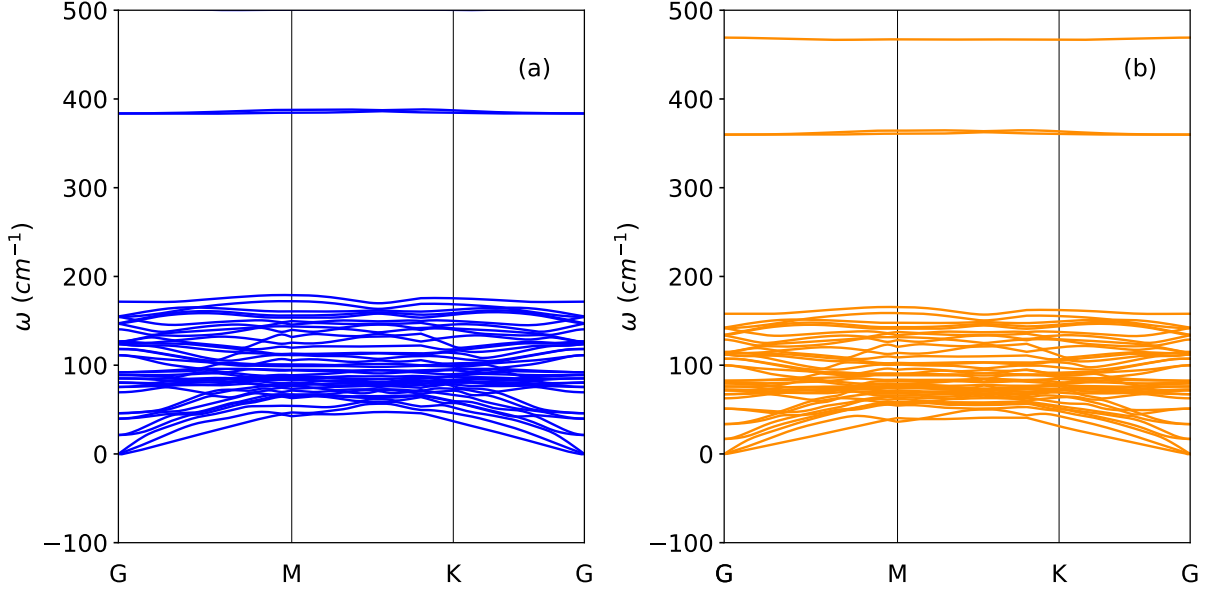


Figure 17: Phonon dispersion for the $\text{CO}_{\text{top}}/\text{Pt}(111)$ configuration calculated with (a) PBE (blue) and (b) vdW-DF (orange) using a \mathbf{q} -grid of $6 \times 6 \times 1$.

4.4 Thermal Conditions

In this section we analyze the temperature dependence of the IS mode spectra under thermal equilibrium conditions, *i.e.*, under conditions in which electrons and phonons are characterized by the same temperature ($T_e = T_l = T$).

The temperature dependence of the IS linewidth in the range $T \in [0, 350 \text{ K}]$ is shown in Fig. 18(a) for each functional with solid lines and squares: PBE (blue), vdW-DF (orange) and BEEF-vdW (green). Also shown in the same figure are the two experimental values we found in the literature for 0.33 ML and two different temperatures, $\gamma \approx 9 \text{ cm}^{-1}$ at 150 K (brown triangle) [66] and $\gamma \approx 6 \text{ cm}^{-1}$ at 300 K (purple triangle) [22]. Therefore, considering the dispersion of these two experimental values, the values of the linewidth obtained with the three xc functionals can be considered to be in reasonable agreement with experiments. For illustrative purposes, we also show in the same figure the experimental results of $\gamma(T)$ measured for a coverage of 0.5 ML [67] (red dots and solid line). In principle, the linewidth is expected to decrease as the coverage increases [66]. Thus, the comparison with the theoretical linewidths should remain at a qualitative level. In this respect, note that the linewidth increases with T as also predicted by our calculations. The theoretical dependence is more pronounced, but we cannot exclude coverage effects in doing this qualitative comparison also.

Figure 18(a) also shows the first-order contribution to the linewidth, $\gamma^{[1]}(T)$ [see Eq. (44)], in dashed-lines and squares for the three functionals: PBE (blue), vdW-DF (orange), and BEEF-vdW (green). This analysis covers the same temperature range as the total

linewidth and exhibits the expected nearly constant dependence on temperature. In CO/Pd(111) [59], the authors also observed a constant behavior in the first-order linewidth of the CO IS mode for temperatures ranging from 0 to 300 K. Note that the T dependence is ruled by the Fermi-Dirac distribution that remains almost unchanged within this temperature range. The first-order term dominates the linewidth at very low temperatures ($T < 100$ K). As the temperature increases, the contribution of the second-order term $\gamma^{[2]}(T)$ (Eq.(45)) in the total linewidth becomes more and more important. As shown in the figure, the temperature dependence of the total linewidth is in fact governed by this term accounting for the electron-mediated phonon-phonon coupling (EMPPC) processes (see section 2.3.2). For CO/Pd(111) [59] and CO/Cu(100) [12] at low temperatures, a T^3 dependence of γ was observed up to approximately 160 K, transitioning to a linear behavior afterwards. In the case of CO/Pt(111), the linear dependence appears already at a very low temperature and describes the whole temperature range shown in the figure.

Regarding the dependence of the linewidth on the different xc functionals, the first-order term differs in 1 cm^{-1} . The largest value is predicted by BEEF-vdW ($\gamma^{[1]}(T = 0) = 5.6 \text{ cm}^{-1}$), followed by the similar values of vdW-DF and PBE ($\gamma^{[1]}(T = 0) = 4.9 \text{ cm}^{-1}$ and 4.6 cm^{-1} , respectively). The differences in the total linewidth become more apparent as T increases and are ruled by the different T dependence of the second-order EMPPC term. In particular, the largest slope corresponds to vdW-DF followed by PBE and BEEF-vdW, in this order.

Finally, the temperature-dependent IS frequency shift, $\Delta\omega(T) = \omega(T) - \omega(0)$, is plotted in Figure 18(b) within the temperature range $T \in [0, 350]$ K for the three functionals: PBE (blue squares and solid lines), vdW (orange squares and solid lines), and BEEF-vdW (green squares and solid lines). Additionally, we include the experimental results of $\Delta\omega(T)$ for 0.5 ML [67] (red dots and solid lines). As expected, the changes in $\Delta\omega^{[1]}$ are minimal across the temperature range $T \in [0, 350]$ K, specifically $\Delta\omega^{[1]} \approx 0.15 \text{ cm}^{-1}$. This negligible contribution of the first-order frequency shift is also consistent with observations made for CO/Pd(111) [59]. As in the case of the linewidth, the main factor responsible for the increasing frequency redshift of the IS mode is the second-order EMPPC term. The rate of increase in $\Delta\omega(T)$ is the highest for vdW-DF, followed by PBE and BEEF-vdW, respectively. Remarkably, the increasing redshift of the frequency with temperature is also experimentally confirmed, as indicated by the red dots in the plot. Note however that, as remarked above, the experiments are performed for a different CO coverage and, therefore, the comparison should be qualitative rather than quantitative.

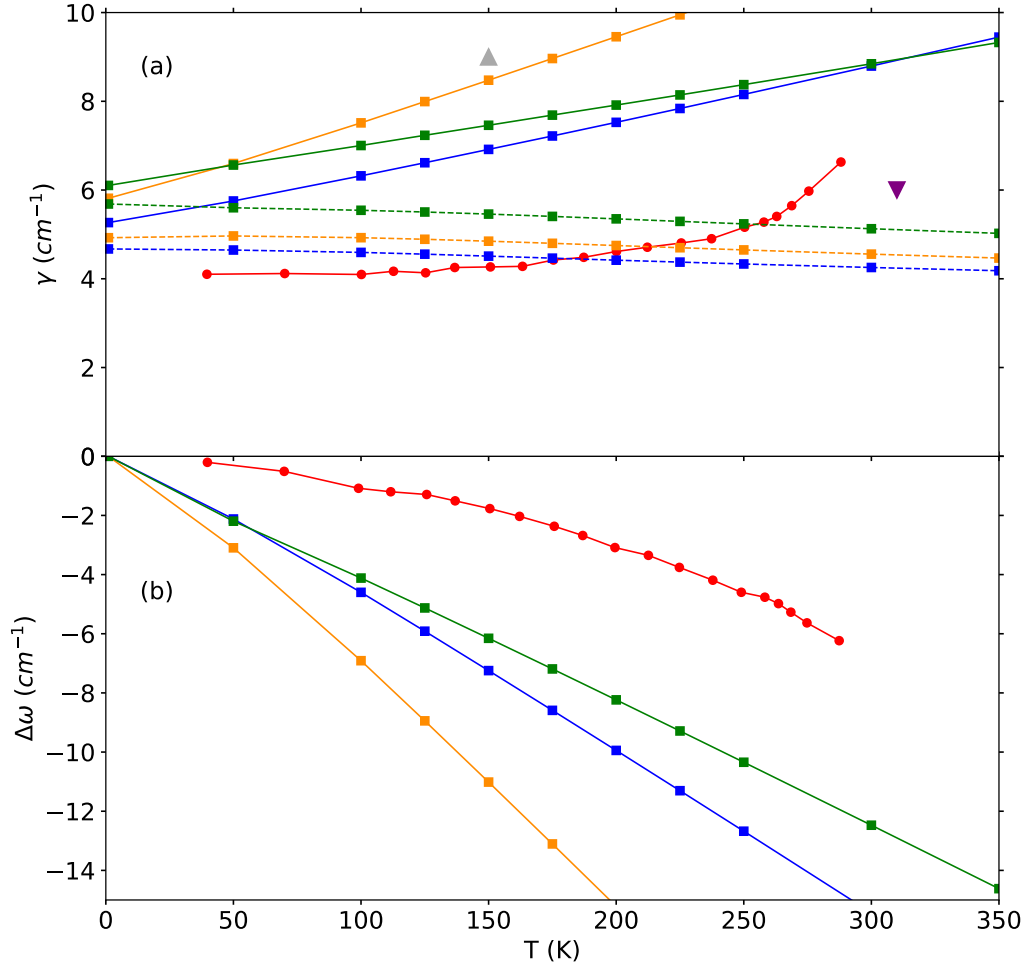


Figure 18: Temperature dependence of the CO IS vibrational mode for $\text{CO}_{\text{top}}/\text{Pt}(111)$ as obtained with PBE (blue), vdW-DF (orange) and BEEF-vdW (green). (a) Total linewidth $\gamma(T)$ (solid lines and squares) and experimental values from [67] for a 0.5 ML coverage (red dots) and from [22] (purple triangle) and [66] (grey triangle) for 0.33 ML coverage. For each xc functional, the first-order linewidth $\gamma^{[1]}(T)$ is plotted with dashed lines and squares. (b) Total frequency shift $\Delta\omega(T)$ (see text) and experimental values from [67] (red dots). Note here that we subtract 2106 cm^{-1} (experimental value at $T \approx 50 \text{ K}$) to all the experimental data of $\Delta\omega(T)$.

4.5 Non-Equilibrium Conditions

In this section we analyze the transient changes in the CO IS vibrational spectra when the $\text{CO}_{\text{top}}/\text{Pt}(111)$ system is pumped with a 400 nm laser pulse with 150 fs duration. We consider that the pulse peak intensity hits the surface at $t = 0 \text{ fs}$ and the system is initially in thermal equilibrium at $T = 90 \text{ K}$. Using these common conditions, the transient IS

spectra is calculated for three absorption fluences, namely, $F = 40, 80$, and 130 J/m^2 . Let us remark that these are the experimental conditions and laser properties of the TR-IVSFG experiments conducted by Watanabe *et al.* [2] for the CO/Pt(111) system with a coverage of 0.33 ML. Figures 19(a) and (b) reproduce the time-evolution of the IS linewidth and frequency shift observed in these experiments for the three fluences. As shown in the figure, the spectral changes increase with the laser fluence. In the case of the linewidth, there is a common initial decrease respect to the reference value of about 5 cm^{-1} that is measured before exciting the system with the pump pulse. Next, γ increases rapidly within a time interval of about 1–1.5 ps and starts to decrease reaching a steady stage in which the value remains basically constant. In the case of the frequency there is a fast initial redshift that last 1-1.5 ps, followed by a slower blueshift that coincides in time with the steady stage reached by the linewidth. Next, we proceed to discuss the result of our calculations for these experimental conditions.

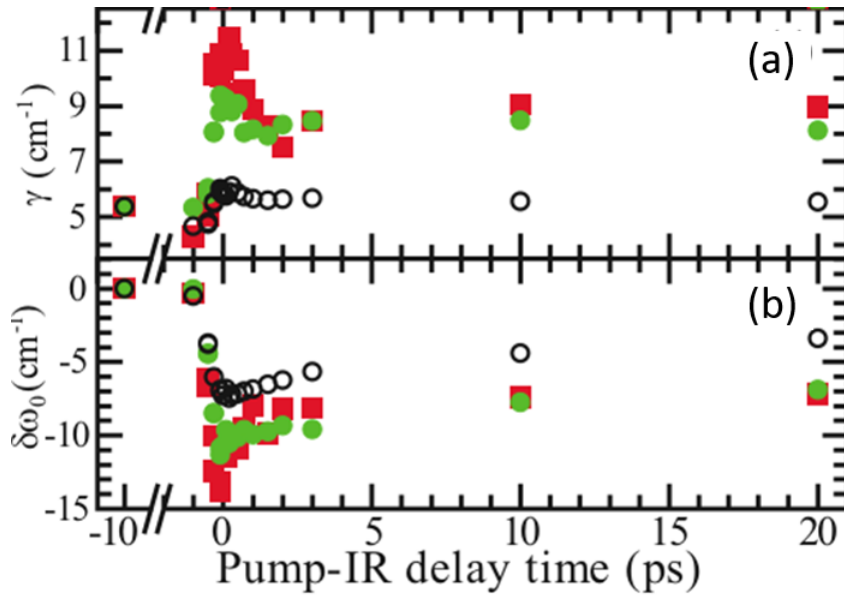


Figure 19: *Transient spectra reported in Ref. [2] for the IS phonon mode of CO adsorbed on Pt(111) with a coverage 0.33 ML. (a) Linewidth and (b) frequency shift against the Pump-IR delay time for absorption fluences: 40 (open circles), 80 (green squares), and 130 J/m^2 (red squares). Figure reproduced from Phys. Rev. B **81**, 241408 (R) (2010).*

As explained in section 3.6, the excitation created in the system by the 400 nm pump pulse is described within a two-temperature model in terms of two-coupled thermal baths, one describing the laser-induced excited electrons that is characterized by a temperature $T_e(t)$ and another one with temperature $T_l(t)$ describing the excited phonons that result from the coupling to the hot electrons. The time evolution of the transient IS spectra is obtained by inserting these time-dependent temperatures in the expressions of the first- (Eq. (37)) and second-order (Eq. (38)) self-energy. Recall that $\pi^{[1]}$ depends only on $T_e(t)$, while $\pi^{[2]}$ depends on $T_e(t)$ and $T_l(t)$. As presented by Watanabe *et al.*, we compute the frequency shift $\Delta\omega(t)$ and the linewidth $\gamma(t)$. To do so, we make use of Eqs. (42)-(45). Let us start remarking that the vdw-DF results are not included in this section because, compared to both our PBE and BEEF-vdW results and the experimental data, this

functional is yielding significantly larger values for the linewidth and frequency shift. A preliminary analysis of the results indicate that the contribution of the low frequency phonons to the EMPPC term is somehow overestimated. Further calculations are still in progress to exclude possible numerical errors when evaluating the electron-phonon matrix elements in this case.

The time evolution of the IS linewidth and frequency shift calculated with PBE and BEEF-vdW for the experimental fluences are shown in Figs. 20 and 21, respectively. In general, the time evolution and fluence dependence of $\gamma(t)$ and $\Delta\omega(t)$ obtained with PBE and BEEF-vdW are qualitatively similar. A common feature is that PBE yields larger values than BEEF-vdW for both $\gamma(t)$ and $\Delta\omega(t)$. In agreement with experiments, the magnitude of the two quantities increases with the laser fluence, but the experimental values, particularly in the steady regime ($t > 1$ ps), are systematically overestimated. We recognize important common features between theory and experiments though. In the case of the linewidth (Figs. 20(a) and 21(a)), both PBE and BEEF-vdW reproduce the initial decay occurring around $t = 0$ ps followed by the rapid increase that gives rise to the peak structures in experiments. The important difference refers to the subsequent steady regime that is clearly overestimated by both xc functionals. With BEEF-vdW, for example, the linewidth values in the interval $t = 5 - 10$ ps are about 10, 12, and 14 cm^{-1} for $F = 40, 80$, and 130 J/m^{-2} , whereas in experiments $\gamma = 6, 8$, and 10 cm^{-1} , respectively.

Regarding the frequency shift (Figs. 20(b) and 21(b)), we observe a consistent redshift for both functionals, which eventually decreases slowly in magnitude (blueshift) at longer times, as observed in experiments. Similar to the linewidth, however, our theoretical results exhibit much larger values than the experimental ones during the steady regime. For instance, in the experimental results, changes in $\Delta\omega$ around $-5, -7$, and -9 cm^{-1} are observed for $F = 40, 80$, and 130 J/m^2 in the interval $t = 5 - 10$ ps, whereas the corresponding PBE values are around $-17, -30$, and -40 cm^{-1} and around $-14, -22$, and -32 cm^{-1} for BEEF-vdW. These large values at longer times are possibly masking the peak structure observed in experiments for 80 and 130 J/m^2 . For the latter fluence, note that there is an incipient peak for both PBE and BEEF-vdW at $t \approx 0.3$ fs.

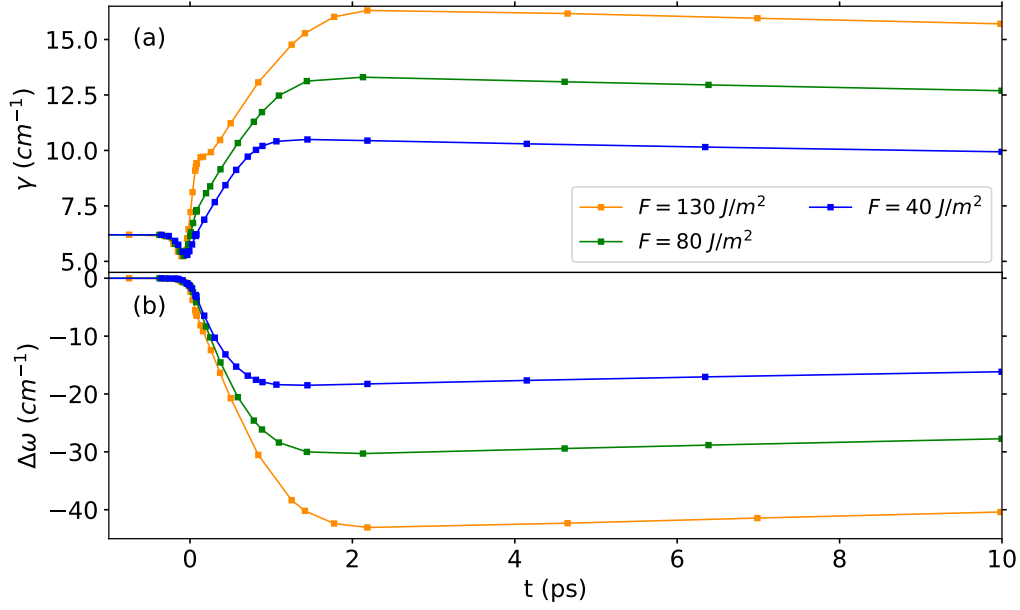


Figure 20: Transient changes in the IS vibrational spectra of $\text{CO}_{\text{top}}/\text{Pt}(111)$ calculated with PBE for a 400 nm laser pump pulse with 150 fs duration and peak intensity hitting the system at $t = 0$ ps. The initial system temperature is 90 K. (a) Linewidth and (b) frequency shift as a function of time for absorbed fluences $F = 40$ (blue), 80 (green), and 130 J/m^2 (orange).

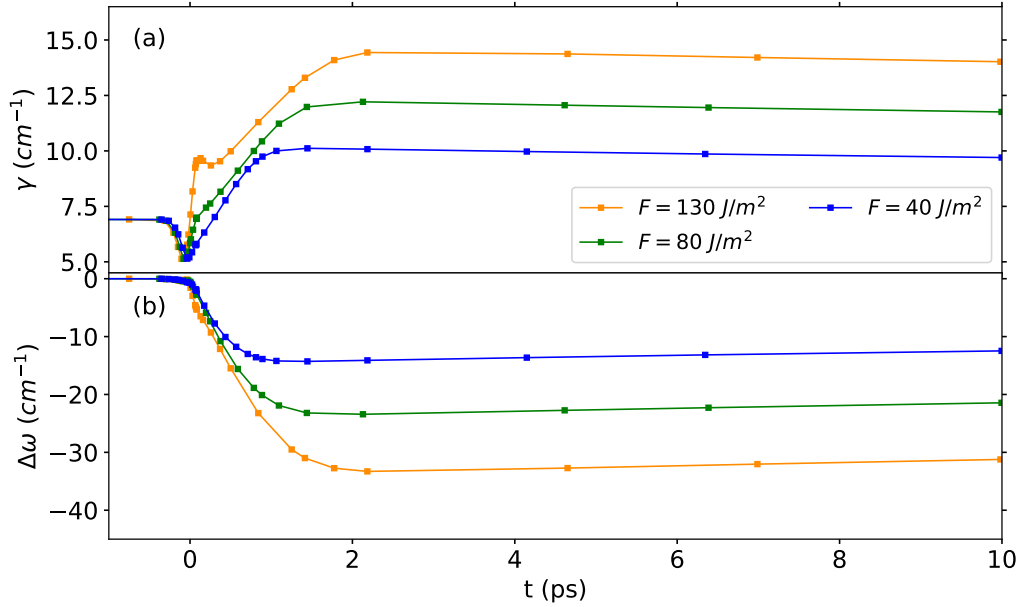


Figure 21: Same as Fig. 20 for BEEF-vdW.

To understand how the first- and second-order processes contribute to the time evolution of the IS spectra and to find what causes the discrepancy between theory and experiments, we show in Fig. 22 the contribution of first-order processes (dashed lines and squares) to

both $\Delta\gamma(t)$ and $\Delta\omega(t)$ (solid lines and squares) for $F = 40 \text{ J/m}^{-2}$ (top 3-panels, (a)-(c)), 80 J/m^{-2} (middle 3-panels, (d)-(f)), and 130 J/m^{-2} (bottom 3-panels, (g)-(i)). For each fluence, the top panel shows the corresponding electronic and phononic temperature, $T_e(t)$ and $T_l(t)$, the middle panel shows $\Delta\gamma(t)$, and the bottom panel $\Delta\omega(t)$.

Figures 22(b), (e), and (h) show that the initial decrease in $\Delta\gamma(t)$ that is obtained for the three fluences is due to the first-order term $\Delta\gamma^{[1]}$ (dashed-lines and squares) that decays rapidly as T_e begins to rise (see the corresponding $T_e(t)$ in Figures 22(a), (d), and (g)). This decay is followed by a rapid increase, resulting in a γ change of approximately 4 cm^{-1} with PBE and 3 cm^{-1} with BEEF-vdW for $F = 40 \text{ J/m}^2$; 7 cm^{-1} (PBE) and 6 cm^{-1} (BEEF-vdW) for $F = 80 \text{ J/m}^2$; and 10 cm^{-1} (PBE) and 7 cm^{-1} (BEEF-vdW) for $F = 130 \text{ J/m}^2$. In this second regime, the second-order EMPPC processes ($\gamma^{[2]}$) dominate the total linewidth change. Note lastly, that the frustrated peaks that appear in $\Delta\gamma(t)$ at absorbed fluences of 80 and 130 J/m^2 coincide in time with the instant at which $T_e(t)$ is the highest and are also a consequence of the peculiar behaviour followed by $\Delta\gamma^{[1]}$.

Finally, Figs. 22(c), (f), and (i) show for the three fluences that the first-order term ($\Delta\omega^{[1]}$ represented by dashed lines and squares) initially experiences a blueshift as T_e begins to rise, reaching its maximum when T_e is at its highest value. However, this blueshift is in all cases masked by the second-order term $\Delta\omega^{[2]}$ that dominates throughout the entire process, resulting in a redshift during the whole time interval. In the case of CO/Pd(111) [59], two distinct regimes in $\Delta\omega(t)$ are observed: initially, a rapid blueshift caused by the dominance of $\Delta\omega^{[1]}$ during the initial 0.5 ps and next a transition to a steady redshift that is completed during the approximately initial 1–1.5 ps. The redshift is due to the second-order EMPPC processes. The absence of blueshift in CO/Pt(111) is a consequence of the clear dominance of the EMPPC processes throughout the entire time interval that last the perturbation created by the pump pulse.

In summary, our findings demonstrate a persistent redshift across all three functionals for fluences of 40, 80, and 130 J/m^2 , consistent with the observations in TR-IVSFG experiments performed in this system [2]. Although $\Delta\omega^{[1]}$ initially exhibits a blueshift, the dominant contribution of the EMPPC process ultimately leads to a redshift. It is worth noting that our calculated values for the total change in linewidth and frequency shift are generally overestimating for all fluences and functionals the experimental values. Among the functionals, vdW-DF yields the largest values, followed by PBE, and next BEEF-vdW. The quantitative discrepancy between theory and experiments arises from the fact that both $\gamma^{[2]}$ and $\Delta\omega^{[2]}$ take rather large values when compared to experimental data.

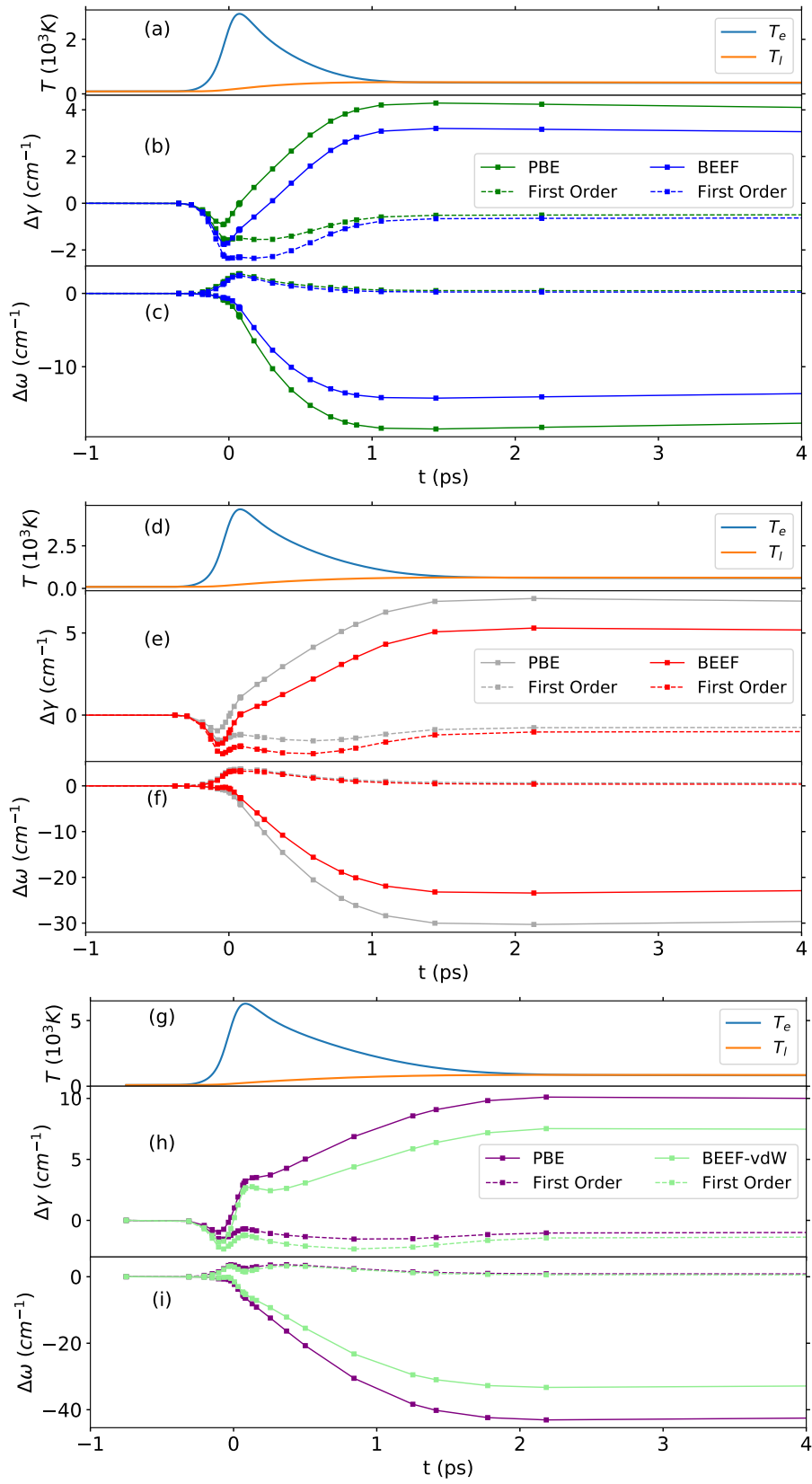


Figure 22: Time evolution of the electronic $T_e(t)$ (cyan) and lattice $T_l(t)$ (orange) temperatures, the linewidth change $\Delta\gamma(t)$, and the frequency shift $\Delta\omega(t)$ for $F = 40 \text{ J/m}^2$ (panels (a)-(c), respectively), $F = 80 \text{ J/m}^2$ (panels (d)-(f)), and $F = 130 \text{ J/m}^2$ (panels (g)-(i)). Total changes in solid-lines and squares and first-order contributions in dashed-lines and squares. Laser properties as in Fig. 20.

5 Summary and Conclusions

In summary, the transient changes of the internal stretch mode spectra were studied under thermal equilibrium conditions and pump-probe non-equilibrium conditions when CO is adsorbed on the top site. The calculations were performed for a coverage of 0.33 ML and for three xc functionals: PBE, vdW-DF, and BEEF-vdW.

Initially, the adsorption energies of CO on Pt(111) were examined for the three exchange-correlation functionals. The results indicated that the preferred adsorption position using PBE was the hollow site (hcp), while the top site was favored when employing vdW-DF. On the other hand, the results for BEEF-vdW indicated a preference for the hollow site (fcc).

The study continued by examining the projected electronic density of states for surface atoms in the presence of an adsorbed CO molecule on both the top and hcp sites, specifically for PBE. Previous research has highlighted significant differences in the DOS of CO/Pt(111) depending on the adsorption site, including fcc, hcp, bridge, and top [63]. In our results, it was observed that when CO binds to the top site, a strong interaction occurs between the CO molecule and the d_{z^2} and s orbitals of the Pt atom directly below it, resulting in a shift of these Pt-projected DOS towards lower energies. The orbital interaction was observed between the CO molecular orbital with σ character and the Pt s and d_{z^2} orbitals. Additionally, it was observed that the CO MOs with π_x and π_y character predominantly interact with the $d_{zx} + d_{zy}$ orbitals of Pt. Respect to hcp adsorption site, the coupling between the CO MOs and the d_{z^2} orbital of Pt was absent.

Furthermore, an study was conducted on the vibrational spectra of the CO molecule adsorbed on Pt(111), identifying the Internal Stretch (IS) and External Stretch (ES) vibrational modes. In the case of BEEF-vdW, negative frequencies were observed when the CO molecule was adsorbed on the top site, suggesting the presence of unstable vibrational modes. These unstable modes were attributed to frustrated translations of the CO molecule. To verify the stability of the CO_{top}/Pt(111) configuration using PBE and vdW-DF, the phonon-dispersion was computed and no negative frequencies were observed. When CO was adsorbed on the fcc site (which was found to be the most favorable site according to BEEF-vdW), no negative vibrational modes were obtained, indicating a stable adsorption position. Additionally, the frequencies of the IS and ES modes were observed to shift to lower values.

Afterward, the temperature dependence of the internal stretch mode spectra was calculated for the case of thermal equilibrium conditions (i.e., for equal electron and phonon temperatures). A linear behavior in the total linewidth with temperature was obtained for the three xc functionals. Furthermore, the first order contribution to the linewidth, $\gamma^{[1]}$, exhibited a small linear response, while the second-order term $\gamma^{[2]}$ gained significance as temperature grows. It was concluded that the increasing frequency redshift of the IS mode primarily resulted from the EMPPC process. The experimental result for 0.33 ML at 150 K agrees rather well with our computational findings. Existing experiments for 0.5 ML confirmed the tendency of the frequency shift to increase (in absolute values) with temperature.

Finally, the transient changes induced in the vibrational spectra of $\text{CO}_{\text{top}}/\text{Pt}(111)$ by a 400 nm laser pump pulse were also studied. Three different absorption fluences were considered: 40, 80, and 130 J/m².

The three xc functionals predicted a transient increase in the linewidth and frequency shift to larger values (in absolute value, i.e., a redshift) for all the absorbed fluences, which were consistent with the observations in time-resolved infrared-visible sum-frequency-generation spectroscopy experiments [2]. It is worth noting that the calculated values for the total change in linewidth and frequency shift were generally overestimating the experimental values for all fluences and xc functionals, from the fact that both $\gamma^{[2]}$ and $\Delta\omega^{[2]}$ took rather large values when compared to experimental data. Among the xc functionals, vdW-DF yields the largest values, followed by PBE, and next BEEF-vdW.

Further research could be conducted to enhance the accuracy of our calculations in this Master Thesis. Computing calculations for thermal equilibrium a pump probe non-equilibrium conditions for other adsorption sites (fcc, hcp and bridge) would provide insights into whether the overestimation of $\gamma^{[2]}$ and $\Delta\omega^{[2]}$ persists across different adsorption sites. Calculations could be also conducted for different coverages, so that the computational results could be compared over a wider range of experimental values. Additionally, exploring a larger surface slab (for example containing 6 layers instead of 4) would be intriguing to evaluate the importance of finite size effects in the calculations that we present here.

References

- [1] H. Arnolds and M. Bonn, “Ultrafast surface vibrational dynamics,” *Surface Science Reports*, vol. 65, no. 2, pp. 45–66, 2010.
- [2] K. Watanabe, K.-i. Inoue, I. F. Nakai, and Y. Matsumoto, “Nonadiabatic coupling between co stretching and pt substrate electrons enhanced by frustrated mode excitations,” *Physical Review B*, vol. 81, no. 24, p. 241408, 2010.
- [3] T. A. Germer, J. C. Stephenson, E. J. Heilweil, and R. R. Cavanagh, “Hot carrier excitation of adlayers: Time-resolved measurement of adsorbate-lattice coupling,” *Physical Review Letters*, vol. 71, p. 3327, 1993.
- [4] M. Bonn, C. Hess, S. Funk, J. H. Miners, B. N. J. Persson, M. Wolf, and G. Ertl, “Femtosecond surface vibrational spectroscopy of CO adsorbed on Ru(001) during desorption,” *Physical Review Letters*, vol. 84, pp. 4653–4656, May 2000.
- [5] E. H. G. Backus, A. Eichler, A. W. Kleyn, and M. Bonn, “Real-time observation of molecular motion on a surface,” *Science*, vol. 310, no. 5755, p. 1790, 2005.
- [6] K.-i. Inoue, K. Watanabe, and Y. Matsumoto, “Instantaneous vibrational frequencies of diffusing and desorbing adsorbates: Co/pt (111),” *The Journal of Chemical Physics*, vol. 137, no. 2, p. 024704, 2012.
- [7] I. M. Lane, Z.-P. Liu, D. A. King, and H. Arnolds, “Ultrafast vibrational dynamics of no and co adsorbed on an iridium surface,” *The Journal of Physical Chemistry C*, vol. 111, no. 38, pp. 14198–14206, 2007.
- [8] K.-i. Inoue, K. Watanabe, T. Sugimoto, Y. Matsumoto, and T. Yasuike, “Disentangling multidimensional nonequilibrium dynamics of adsorbates: Co desorption from cu (100),” *Physical Review Letters*, vol. 117, no. 18, p. 186101, 2016.
- [9] J. Cook, S. Clowes, and E. McCash, “Reflection absorption ir studies of vibrational energy transfer processes and adsorption energetics,” *Journal of the Chemical Society, Faraday Transactions*, vol. 93, no. 13, pp. 2315–2322, 1997.
- [10] B. Persson and R. Ryberg, “Vibrational phase relaxation at surfaces: Co on ni (111),” *Physical Review Letters*, vol. 54, no. 19, p. 2119, 1985.
- [11] T. Omiya, Y. Kim, R. Raval, and H. Arnolds, “Ultrafast vibrational dynamics of co ligands on rutpp/cu (110) under photodesorption conditions,” *Surfaces*, vol. 2, no. 1, pp. 117–130, 2019.
- [12] D. Novko, M. Alducin, and J. I. Juaristi, “Electron-mediated phonon-phonon coupling drives the vibrational relaxation of co on cu (100),” *Physical Review Letters*, vol. 120, no. 15, p. 156804, 2018.
- [13] D. Novko, J. C. Tremblay, M. Alducin, and J. Juaristi, “Ultrafast transient dynamics of adsorbates on surfaces deciphered: The case of co on cu (100),” *Physical Review Letters*, vol. 122, no. 1, p. 016806, 2019.

- [14] R. Bombín, A. S. Muzas, D. Novko, J. I. Juaristi, and M. Alducin, “Anomalous transient blueshift in the internal stretch mode of co/pd (111),” *Physical Review B*, vol. 107, no. 12, p. L121404, 2023.
- [15] A. Kokalj and M. Causà, “Periodic density functional theory study of pt (111): surface features of slabs of different thicknesses,” *Journal of Physics: Condensed Matter*, vol. 11, no. 39, p. 7463, 1999.
- [16] N. W. Ashcroft and N. D. Mermin, *Solid state physics*. Cengage Learning, 2022.
- [17] H. Froitzheim, H. Hopster, H. Ibach, and S. Lehwald, “Adsorption sites of co on pt (111),” *Applied Physics*, vol. 13, no. 2, pp. 147–151, 1977.
- [18] H. Hopster and H. Ibach, “Adsorption of co on pt (111) and pt 6 (111)×(111) studied by high resolution electron energy loss spectroscopy and thermal desorption spectroscopy,” *Surface Science*, vol. 77, no. 1, pp. 109–117, 1978.
- [19] A. Baro and H. Ibach, “New study of co adsorption at low temperature (90 k) on pt (111) by eels,” *The Journal of Chemical Physics*, vol. 71, no. 12, pp. 4812–4816, 1979.
- [20] G. Ertl, M. Neumann, and K. Streit, “Chemisorption of co on the pt (111) surface,” *Surface Science*, vol. 64, no. 2, pp. 393–410, 1977.
- [21] H. J. Krebs and H. Lüth, “Evidence for two different adsorption sites of co on pt (111) from infrared reflection spectroscopy,” *Applied Physics*, vol. 14, pp. 337–342, 1977.
- [22] A. Crossley and D. A. King, “Infrared spectra for co isotopes chemisorbed on pt “111”: Evidence for strong adsorbate coupling interactions,” *Surface Science*, vol. 68, pp. 528–538, 1977.
- [23] K. Horn and J. Pritchard, “Infrared spectra of ordered and disordered overlayers on metals: Carbon monoxide on a platinum (111) single crystal surface,” *Le Journal de Physique Colloques*, vol. 38, no. C4, pp. C4–164, 1977.
- [24] P. Norton, J. Goodale, and E. Selkirk, “Adsorption of co on pt (111) studied by photoemission, thermal desorption spectroscopy and high resolution dynamic measurements of work function,” *Surface Science*, vol. 83, no. 1, pp. 189–227, 1979.
- [25] B. Persson and R. Ryberg, “Vibrational line shapes of low-frequency adsorbate modes: Co on pt (111),” *Physical Review B*, vol. 40, no. 15, p. 10273, 1989.
- [26] Y. T. Wong and R. Hoffmann, “Chemisorption of carbon monoxide on three metal surfaces: nickel(111), palladium(111), and platinum(111): a comparative study,” *The Journal of Physical Chemistry*, vol. 95, no. 2, pp. 859–867, 1991.
- [27] Y. Morikawa, J. J. Mortensen, B. Hammer, and J. K. Nørskov, “Co adsorption and dissociation on pt (111) and ni (111) surfaces,” *Surface Science*, vol. 386, no. 1-3, pp. 67–72, 1997.
- [28] P. J. Feibelman, B. Hammer, J. K. Nørskov, F. Wagner, M. Scheffler, R. Stumpf, R. Watwe, and J. Dumesic, “The co/pt (111) puzzle,” *The Journal of Physical Chemistry B*, vol. 105, no. 18, pp. 4018–4025, 2001.

- [29] R. Olsen, P. Philipson, and E. Baerends, “Co on pt (111): A puzzle revisited,” *The Journal of Chemical Physics*, vol. 119, no. 8, pp. 4522–4528, 2003.
- [30] G. Kresse, A. Gil, and P. Sautet, “Significance of single-electron energies for the description of co on pt (111),” *Physical Review B*, vol. 68, no. 7, p. 073401, 2003.
- [31] P. Janthon, F. Vines, J. Sirijaraensre, J. Limtrakul, and F. Illas, “Adding pieces to the co/pt (111) puzzle: the role of dispersion,” *The Journal of Physical Chemistry C*, vol. 121, no. 7, pp. 3970–3977, 2017.
- [32] Y. Zhao and D. G. Truhlar, “A new local density functional for main-group thermochemistry, transition metal bonding, thermochemical kinetics, and noncovalent interactions,” *The Journal of Chemical Physics*, vol. 125, no. 19, p. 194101, 2006.
- [33] M. Dion, H. Rydberg, E. Schröder, D. C. Langreth, and B. I. Lundqvist, “Van der waals density functional for general geometries,” *Physical Review Letters*, vol. 92, no. 24, p. 246401, 2004.
- [34] G. K. K. Gunasooriya and M. Saeys, “Co adsorption on pt (111): from isolated molecules to ordered high-coverage structures,” *ACS Catalysis*, vol. 8, no. 11, pp. 10225–10233, 2018.
- [35] I. Kundappaden, R. Chatanathodi, *et al.*, “A dft study of co adsorption on pt (111) using van der waals functionals,” *Surface Science*, vol. 681, pp. 143–148, 2019.
- [36] É. D. Murray, K. Lee, and D. C. Langreth, “Investigation of exchange energy density functional accuracy for interacting molecules,” *Journal of Chemical Theory and Computation*, vol. 5, no. 10, pp. 2754–2762, 2009.
- [37] E. Engel and R. M. Dreizler, “Density functional theory,” *Theoretical and Mathematical Physics*, pp. 351–399, 2011.
- [38] D. Novko, *Nonadiabatic effects in adsorbate-surface interactions from first principles*. PhD thesis, Universidad del País Vasco, 2017.
- [39] W. Kohn and L. J. Sham, “Self-consistent equations including exchange and correlation effects,” *Physical Review*, vol. 140, no. 4A, p. A1133, 1965.
- [40] R. M. Martin, *Electronic structure: basic theory and practical methods*. Cambridge university press, 2020.
- [41] P. A. Dirac, “Note on exchange phenomena in the thomas atom,” in *Mathematical proceedings of the Cambridge philosophical society*, vol. 26, pp. 376–385, Cambridge University Press, 1930.
- [42] M. A. Marques, M. J. Oliveira, and T. Burnus, “Libxc: A library of exchange and correlation functionals for density functional theory,” *Computer Physics Communications*, vol. 183, no. 10, pp. 2272–2281, 2012.
- [43] D. M. Ceperley and B. J. Alder, “Ground state of the electron gas by a stochastic method,” *Physical Review Letters*, vol. 45, no. 7, p. 566, 1980.

- [44] J. P. Perdew, K. Burke, and M. Ernzerhof, “Generalized gradient approximation made simple,” *Physical Review Letters*, vol. 77, no. 18, p. 3865, 1996.
- [45] J. Wellendorff, K. T. Lundgaard, A. Møgelhøj, V. Petzold, D. D. Landis, J. K. Nørskov, T. Bligaard, and K. W. Jacobsen, “Density functionals for surface science: Exchange-correlation model development with bayesian error estimation,” *Physical Review B*, vol. 85, no. 23, p. 235149, 2012.
- [46] F. Giustino, “Electron-phonon interactions from first principles,” *Reviews of Modern Physics*, vol. 89, no. 1, p. 015003, 2017.
- [47] D. Novko, M. Alducin, M. Blanco-Rey, and J. Juaristi, “Effects of electronic relaxation processes on vibrational linewidths of adsorbates on surfaces: The case of co/cu (100),” *Physical Review B*, vol. 94, no. 22, p. 224306, 2016.
- [48] P. Giannozzi, S. Baroni, N. Bonini, M. Calandra, R. Car, C. Cavazzoni, D. Ceresoli, G. L. Chiarotti, M. Cococcioni, I. Dabo, *et al.*, “Quantum espresso: a modular and open-source software project for quantum simulations of materials,” *Journal of Physics: Condensed Matter*, vol. 21, no. 39, p. 395502, 2009.
- [49] P. Giannozzi, O. Andreussi, T. Brumme, O. Bunau, M. B. Nardelli, M. Calandra, R. Car, C. Cavazzoni, D. Ceresoli, M. Cococcioni, *et al.*, “Advanced capabilities for materials modelling with quantum espresso,” *Journal of Physics: Condensed Matter*, vol. 29, no. 46, p. 465901, 2017.
- [50] A. Dal Corso, “Pseudopotentials periodic table: From h to pu,” *Computational Materials Science*, vol. 95, pp. 337–350, 2014.
- [51] P. E. Blöchl, “Projector Augmented-wave Method,” *Physical Review B*, vol. 50, pp. 17953–17979, Dec 1994.
- [52] M. Van Hove, N. Materer, U. Starke, A. Barbieri, G. Somorjai, R. Doll, and K. Heinz, “Reliability of detailed leed structural analyses: Pt (111) and pt (111)-p (2x2)-o,” *Surface Science*, vol. 325, no. 3, pp. 207–222, 1995.
- [53] S. Gallego, C. Ocal, and F. Soria, “Surface and bulk reconstruction of pt (111) 1×1 ,” *Surface Science*, vol. 377, pp. 18–22, 1997.
- [54] G. Blackman, M.-L. Xu, D. Ogletree, M. Van Hove, and G. Somorjai, “Mix of molecular adsorption sites detected for disordered co on pt (111) by diffuse low-energy electron diffraction,” *Physical Review Letters*, vol. 61, no. 20, p. 2352, 1988.
- [55] V. Vitale, G. Pizzi, A. Marrazzo, J. R. Yates, N. Marzari, and A. A. Mostofi, “Automated high-throughput wannierisation,” *Npj Computational Materials*, vol. 6, no. 1, p. 66, 2020.
- [56] J. Noffsinger, F. Giustino, B. D. Malone, C.-H. Park, S. G. Louie, and M. L. Cohen, “Epw: A program for calculating the electron–phonon coupling using maximally localized wannier functions,” *Computer Physics Communications*, vol. 181, no. 12, pp. 2140–2148, 2010.

- [57] N. Marzari, A. A. Mostofi, J. R. Yates, I. Souza, and D. Vanderbilt, “Maximally localized wannier functions: Theory and applications,” *Reviews of Modern Physics*, vol. 84, no. 4, p. 1419, 2012.
- [58] S. Anisimov, B. Kapeliovich, T. Perelman, *et al.*, “Electron emission from metal surfaces exposed to ultrashort laser pulses,” *Zh. Eksp. Teor. Fiz*, vol. 66, no. 2, pp. 375–377, 1974.
- [59] R. Bombín, A. S. Muzas, D. Novko, J. I. Juaristi, and M. Alducin, “Vibrational dynamics of co on pd(111) in and out of thermal equilibrium,” *arXiv*, no. 2304.10845[**cond-mat.mtrl-sci**], 2023.
- [60] H. Yokokawa and Y. Takahashi, “Laser-flash calorimetry ii. heat capacity of platinum from 80 to 1000 k and its revised thermodynamic functions,” *The Journal of Chemical Thermodynamics*, vol. 11, no. 5, pp. 411–420, 1979.
- [61] Z. Lin, L. V. Zhigilei, and V. Celli, “Electron-phonon coupling and electron heat capacity of metals under conditions of strong electron-phonon nonequilibrium,” *Physical Review B*, vol. 77, no. 7, p. 075133, 2008.
- [62] Y. Yeo, L. Vattuone, and D. King, “Calorimetric heats for co and oxygen adsorption and for the catalytic co oxidation reaction on pt {111},” *The Journal of Chemical Physics*, vol. 106, no. 1, pp. 392–401, 1997.
- [63] M. Gajdoš, A. Eichler, and J. Hafner, “Co adsorption on close-packed transition and noble metal surfaces: trends from ab initio calculations,” *Journal of Physics: Condensed Matter*, vol. 16, no. 8, p. 1141, 2004.
- [64] Y. Wang, S. de Gironcoli, N. S. Hush, and J. R. Reimers, “Successful a priori modeling of co adsorption on pt (111) using periodic hybrid density functional theory,” *Journal of the American Chemical Society*, vol. 129, no. 34, pp. 10402–10407, 2007.
- [65] C. Adamo and V. Barone, “Toward reliable density functional methods without adjustable parameters: The pbe0 model,” *The Journal of chemical physics*, vol. 110, no. 13, pp. 6158–6170, 1999.
- [66] B. Hayden and A. Bradshaw, “The adsorption of co on pt (111) studied by infrared reflection—absorption spectroscopy,” *Surface Science*, vol. 125, no. 3, pp. 787–802, 1983.
- [67] E. Schweizer, B. Persson, M. Tüshaus, D. Hoge, and A. Bradshaw, “The potential energy surface, vibrational phase relaxation and the order-disorder transition in the adsorption system pt {111}-co,” *Surface Science*, vol. 213, no. 1, pp. 49–89, 1989.